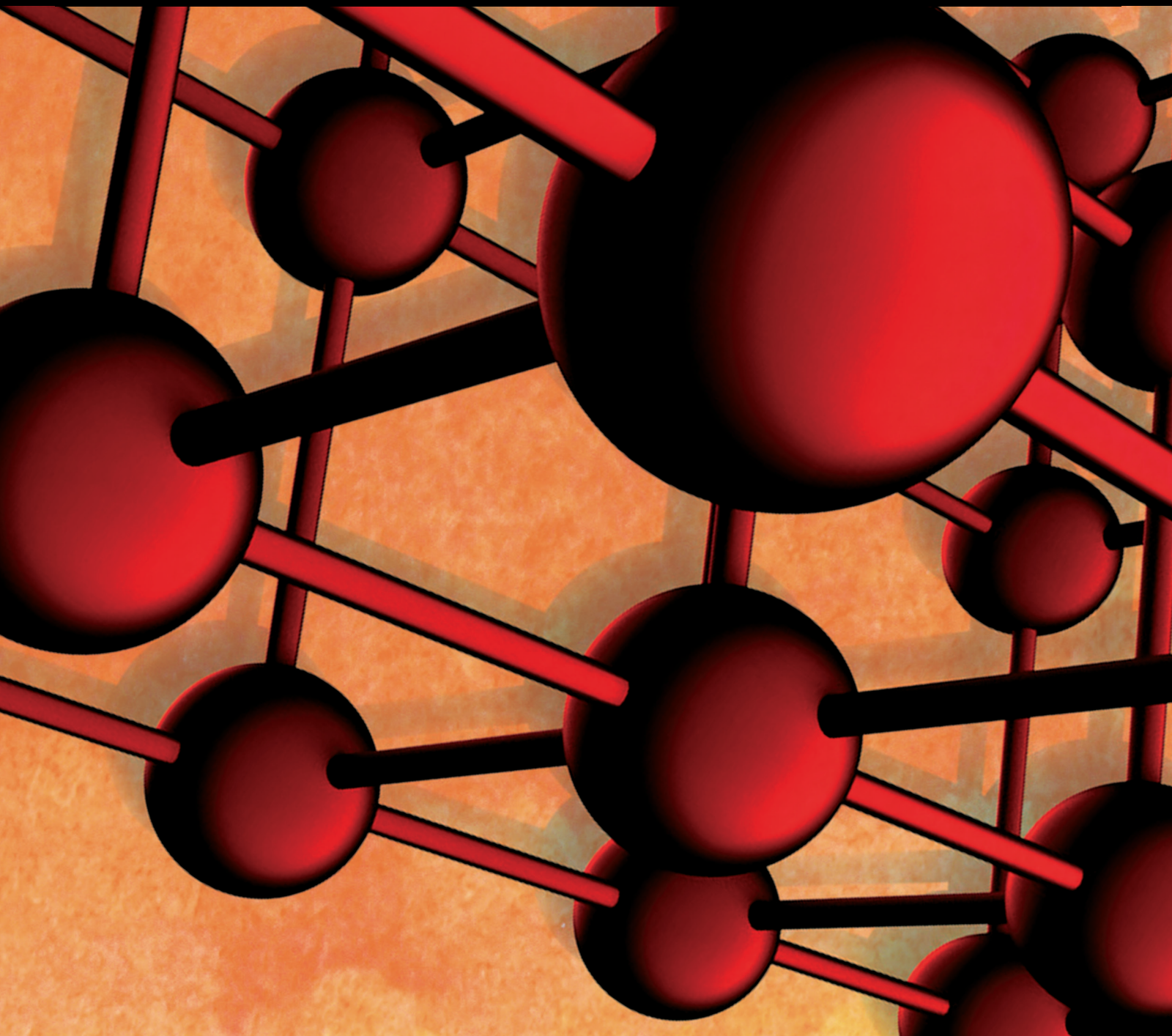


Materials in Built Heritage

Lead Guest Editor: Carlos Alves

Guest Editors: Alexandra Rempel, Ana Soler-Arechalde, and Jorge Sanjurjo-Sánchez





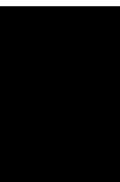
Materials in Built Heritage

Advances in Materials Science and Engineering

Materials in Built Heritage

Lead Guest Editor: Carlos Alves


Guest Editors: Alexandra Rempel, Ana Soler-Arechalde, and Jorge Sanjurjo-Sánchez



Copyright © 2019 Hindawi Limited. All rights reserved.

This is a special issue published in "Advances in Materials Science and Engineering." All articles are open access articles distributed under the Creative Commons Attribution License, which permits unrestricted use, distribution, and reproduction in any medium, provided the original work is properly cited.

Chief Editor











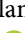








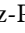








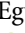
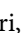
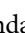
Amit Bandyopadhyay , USA

Associate Editors

Vamsi Balla , India
Mitun Das , USA
Sandip Harimkar, USA
Ravi Kumar , India
Peter Majewski , Australia
Enzo Martinelli , Italy
Luigi Nicolais , Italy
Carlos R. Rambo , Brazil
Michael J. Schütze , Germany
Kohji Tashiro , Japan
Zhonghua Yao , China
Dongdong Yuan , China
Wei Zhou , China

Academic Editors

Antonio Abate , Germany
Hany Abdo , Saudi Arabia
H.P.S. Abdul Khalil , Malaysia
Ismael Alejandro Aguayo Villarreal , Mexico
Sheraz Ahmad , Pakistan
Michael Aizenshtein, Israel
Jarir Aktaa, Germany
Bandar AlMangour, Saudi Arabia
Huaming An, China
Alicia Esther Ares , Argentina
Siva Avudaiappan , Chile
Habib Awais , Pakistan
NEERAJ KUMAR BHOI, India
Enrico Babilio , Italy
Renal Backov, France
M Bahubalendruni , India
Sudharsan Balasubramanian , India
Markus Bambach, Germany
Irene Bavasso , Italy
Stefano Bellucci , Italy
Brahim Benmokrane, Canada
Jean-Michel Bergheau , France
Guillaume Bernard-Granger, France
Giovanni Berselli, Italy
Patrice Berthod , France
Michele Bianchi , Italy
Hugo C. Biscaia , Portugal

Antonio Boccaccio, Italy
Mohamed Bououdina , Saudi Arabia
Gianlorenzo Bussetti , Italy
Antonio Caggiano , Germany
Marco Cannas , Italy
Qi Cao, China
Gianfranco Carotenuto , Italy
Paolo Andrea Carraro , Italy
Jose Cesar de Sa , Portugal
Wen-Shao Chang , United Kingdom
Qian Chen , China
Francisco Chinesta , France
Er-Yuan Chuang , Taiwan
Francesco Colangelo, Italy
María Criado , Spain
Enrique Cuan-Urquizo , Mexico
Lucas Da Silva , Portugal
Angela De Bonis , Italy
Abílio De Jesus , Portugal
José António Fonseca De Oliveira
Correia , Portugal
Ismail Demir , Turkey
Luigi Di Benedetto , Italy
Maria Laura Di Lorenzo, Italy
Marisa Di Sabatino, Norway
Luigi Di Sarno, Italy
Ana María Díez-Pascual , Spain
Guru P. Dinda , USA
Hongbiao Dong, China
Mingdong Dong , Denmark
Frederic Dumur , France
Stanislaw Dymek, Poland
Kaveh Edalati , Japan
Philip Eisenlohr , USA
Luis Evangelista , Norway
Michele Fedel , Italy
Francisco Javier Fernández Fernández , Spain
Spain
Isabel J. Ferrer , Spain
Massimo Fresta, Italy
Samia Gad , Egypt
Pasquale Gallo , Finland
Sharanabasava Ganachari, India
Santiago Garcia-Granda , Spain
Carlos Garcia-Mateo , Spain

Achraf Ghorbal , Tunisia
Georgios I. Giannopoulos , Greece
Ivan Giorgio , Italy
Andrea Grilli , Italy
Vincenzo Guarino , Italy
Daniel Guay, Canada
Jenő Gubicza , Hungary
Xuchun Gui , China
Benoit Guiffard , France
Zhixing Guo, China
Ivan Gutierrez-Urrutia , Japan
Weiwei Han , Republic of Korea
Simo-Pekka Hannula, Finland
A. M. Hassan , Egypt
Akbar Heidarzadeh, Iran
Yi Huang , United Kingdom
Joshua Ighalo, Nigeria
Saliha Ilican , Turkey
Md Mainul Islam , Australia
Iliia Ivanov , USA
Jijo James , India
Hafsa Jamshaid , Pakistan
Hom Kandel , USA
Kenji Kaneko, Japan
Rajesh Kannan A , Democratic People's
Republic of Korea
Mehran Khan , Hong Kong
Akihiko Kimura, Japan
Ling B. Kong , Singapore
Pramod Koshy, Australia
Hongchao Kou , China
Alexander Kromka, Czech Republic
Abhinay Kumar, India
Avvaru Praveen Kumar , Ethiopia
Sachin Kumar, India
Paweł Kłosowski , Poland
Wing-Fu Lai , Hong Kong
Luciano Lamberti, Italy
Fulvio Lavecchia , Italy
Laurent Lebrun , France
Joon-Hyung Lee , Republic of Korea
Cristina Leonelli, Italy
Chenggao Li , China
Rongrong Li , China
Yuanshi Li, Canada




Guang-xing Liang , China
Barbara Liguori , Italy
Jun Liu , China
Yunqi Liu, China
Rong Lu, China
Zhiping Luo , USA
Fernando Lusquiños , Spain
Himadri Majumder , India
Dimitrios E. Manolakos , Greece
Necmettin Maraşlı , Turkey
Alessandro Martucci , Italy
Roshan Mayadunne , Australia
Mamoun Medraj , Canada
Shazim A. Memon , Kazakhstan
Pratima Meshram , India
Mohsen Mhadhbi , Tunisia
Philippe Miele, France
Andrey E. Miroshnichenko, Australia
Ajay Kumar Mishra , South Africa
Hossein Moayedi , Vietnam
Dhanesh G. Mohan , United Kingdom
Sakar Mohan , India
Namdev More, USA
Tahir Muhmood , China
Faisal Mukhtar , Pakistan
Dr. Tauseef Munawar , Pakistan
Roger Narayan , USA
Saleem Nasir , Pakistan
Elango Natarajan, Malaysia
Rufino M. Navarro, Spain
Miguel Navarro-Cia , United Kingdom
Behzad Nematollahi , Australia
Peter Niemz, Switzerland
Hiroschi Noguchi, Japan
Dariusz Oleszak , Poland
Laurent Orgéas , France
Togay Ozbakkaloglu, United Kingdom
Marián Palcut , Slovakia
Davide Palumbo , Italy
Gianfranco Palumbo , Italy
Murlidhar Patel, India
Zbyšek Pavlík , Czech Republic
Alessandro Pegoretti , Italy
Gianluca Percoco , Italy
Andrea Petrella, Italy

Claudio Pettinari , Italy
Giorgio Pia , Italy
Candido Fabrizio Pirri, Italy
Marinos Pitsikalis , Greece
Alain Portavoce , France
Simon C. Potter, Canada
Ulrich Prah, Germany
Veena Ragupathi , India
Kawaljit Singh Randhawa , India
Baskaran Rangasamy , Zambia
Paulo Reis , Portugal
Hilda E. Reynel-Avila , Mexico
Yuri Ribakov , Israel
Aniello Riccio , Italy
Anna Richelli , Italy
Antonio Riveiro , Spain
Marco Rossi , Italy
Fernando Rubio-Marcos , Spain
Francesco Ruffino , Italy
Giuseppe Ruta , Italy
Sachin Salunkhe , India
P Sangeetha , India
Carlo Santulli, Italy
Fabrizio Sarasini , Italy
Senthil Kumaran Selvaraj , India
Raffaele Sepe , Italy
Aabid H Shalla, India
Poorva Sharma , China
Mercedes Solla, Spain
Tushar Sonar , Russia
Donato Sorgente , Italy
Charles C. Sorrell , Australia
Damien Soulat , France
Adolfo Speghini , Italy
Antonino Squillace , Italy
Koichi Sugimoto, Japan
Jirapornchai Suksaeree , Thailand
Baozhong Sun, China
Sam-Shajing Sun , USA
Xiaolong Sun, China
Yongding Tian , China
Hao Tong, China
Achim Trampert, Germany
Tomasz Trzepieciński , Poland
Kavimani V , India

Matjaz Valant , Slovenia
Mostafa Vamegh, Iran
Lijing Wang , Australia
Jörg M. K. Wiezorek , USA
Guosong Wu, China
Junhui Xiao , China
Guoqiang Xie , China
YASHPAL YASHPAL, India
Anil Singh Yadav , India
Yee-wen Yen, Taiwan
Hao Yi , China
Wenbin Yi, China
Tetsu Yonezawa, Japan
Hiroshi Yoshihara , Japan
Bin Yu , China
Rahadian Zainul , Indonesia
Lenka Zaji#c#kova# , Czech Republic
Zhigang Zang , China
Michele Zappalorto , Italy
Gang Zhang, Singapore
Jinghuai Zhang, China
Zengping Zhang, China
You Zhou , Japan
Robert Černý , Czech Republic

Contents

Influence of Hydrophobic Coating on Freeze-Thaw Cycle Resistance of Cement Mortar

Zijian Song , Zhongyuan Lu , and Zhenyu Lai 

Research Article (12 pages), Article ID 8979864, Volume 2019 (2019)

Slurry and Technology Optimization for Grouting Fissures in Earthen Sites with Quicklime

Kai Cui , Fei Feng , Wen-wu Chen , Dong-hua Wang , and Xiao-hai Wang 

Research Article (11 pages), Article ID 9076760, Volume 2019 (2019)

Research Article

Influence of Hydrophobic Coating on Freeze-Thaw Cycle Resistance of Cement Mortar

Zijian Song ^{1,2}, Zhongyuan Lu ¹, and Zhenyu Lai ¹

¹School of Materials Science and Engineering, State Key Laboratory for Environment-Friendly Energy Materials, Southwest University of Science and Technology, Mianyang 621010, China

²Mianyang Vocational and Technical College, Mianyang 621000, China

Correspondence should be addressed to Zijian Song; szj2009189@163.com and Zhongyuan Lu; luy@swust.edu.cn

Received 25 June 2019; Revised 8 August 2019; Accepted 10 October 2019; Published 6 November 2019

Guest Editor: Carlos Alves

Copyright © 2019 Zijian Song et al. This is an open access article distributed under the Creative Commons Attribution License, which permits unrestricted use, distribution, and reproduction in any medium, provided the original work is properly cited.

Due to the porous characteristics of cement-based materials, they are often corroded by salt solutions, which results in decreased durability, especially against damage under freeze-thaw cycles (FTCs). Improving surface properties is an effective way to improve the durability of these materials. In this study, a hydrophobic coating was applied to the surface of cement mortar by chemical modification of low surface energy materials. Fourier transform infrared spectroscopy (FT-IR) showed that low surface energy substances are linked to hydration products through chemical bonds. A water contact angle test indicates that the surface of cement mortar changed from hydrophilic ($\theta=14^\circ$) to hydrophobic ($\theta=140^\circ$) after chemical modification. The cumulative water uptake of hydrophobic samples decreased by 90%. Meanwhile, the wear resistance of the hydrophobic coatings was excellent. Compared with the baseline sample, mass loss rate, flexural strength, and compressive strength of hydrophobic coating samples increased several-fold in the FTC test. Microstructural changes of the mortar were characterized by scanning electron microscopy. The results show that a hydrophobic coating can significantly improve the freeze-thaw resistance of cement-based materials. The formation of a hydrophobic layer on the surface of cement-based materials can improve their durability. The research results not only have applications in civil engineering but will also have great impact in the restoration of historic structures.

1. Introduction

Concrete is a type of building material based on cement with highly effective mechanical properties; it is widely used as a structural material for buildings, bridges, undersea tunnels, etc. In ancient times, cementitious materials made from calcium hydroxide and clay were often used to build what have become today's world-famous historical buildings, such as the Pantheon in Rome. However, both modern and historical buildings are usually corroded by salt solutions, by which water penetrates the concrete, which is a factor contributing to concrete degradation. The freeze-thaw cycle (FTC) in severely frozen regions will cause sustained damage to concrete due to osmotic pressure, water expulsion, and in-pore crystallization during the FTC process [1–6]. Researchers have proposed many methods to improve the FTC resistance of cement-based materials, such as adding air-

entraining substances [7–10], pozzolanic minerals, or fiber admixtures [11–24]. The first method can relieve crystallization pressure in the FTC, while the latter method can improve the compactness of the concrete. However, the aforementioned methods lead to negative impacts on the concrete, such as deteriorating mechanical properties, difficult workability, and increased drying shrinkage.

Super-hydrophobic phenomena exist widely in nature [25–32]. Previous studies have pointed out that two basic requirements must be met for the surface of a solid material to be super-hydrophobic: (1) microscale and nanoscale rough structures and (2) lower surface free energy. Researchers have accurately expressed this theory through the Wenzel model [33] and Cassie-Baxter model [34].

Based on the above research, super-hydrophobic coatings have been applied to concrete surfaces for waterproofing, deicing, and self-cleaning [35–40]. Super-

hydrophobic coatings can be prepared by bonding low surface energy materials to the concrete surface. Materials such as polytetrafluoroethylene (PTFE), polyether ether ketone (PEEK), and silanized diatomaceous earth (DE) are bonded to the concrete surface by epoxy resin to obtain a super-hydrophobic surface [41]. Besides, super-hydrophobic surfaces can also be obtained by bonding super-hydrophobic rice husk ash [42], paper sludge ash [43], or nanosilica gel [34] to the concrete surface. Another way to obtain super-hydrophobic surfaces is the template method, where the features of micropillared molds made of polydimethylsiloxane (PDMS) are replicated immediately after demolding, and then siloxane-based compounds are sprayed to form a low energy surface [44].

Due to the excellent waterproofing effect of super-hydrophobic coatings, the water absorption of concrete decreases significantly, but the durability of such coatings is insufficient and they can easily fall off. Up to now [37], there has been a lack of research on the mechanical stability of super-hydrophobic coatings; therefore, the application of super-hydrophobic coatings in engineering is limited. To solve this problem, a vacuum impregnation process was adopted in this study. Such technology is more suitable for performance improvement of prefabricated concrete structures, similar to the anticorrosion treatment of steel structures. Through this technology, low surface energy materials (iso-octyltriethoxysilane) can penetrate the cement mortar and combine with the cement hydration products, such as calcium hydroxide and ettringite, to form a continuous self-assembled molecular film layer. This molecular film layer reduces the surface energy of the mortar, thus achieving chemical modification of the rough surface of the mortar to form a hydrophobic coating. The wetting property was characterized by a water contact angle (WCA) test. A water absorption test and FTC resistance test were used to evaluate the protective effect of the hydrophobic coating on mortar blocks. Building structures are often subjected to external forces, which may result in surface wear and tear. Thus, the wear resistance was tested by sandpaper polishing under a certain pressure, after which the change of water absorption was tested. The microstructure of the cement mortar was characterized by scanning electron microscopy (SEM). Interface chemical reactions were characterized by Fourier transform infrared spectroscopy (FT-IR).

2. Materials and Methods

2.1. Materials. Ordinary Portland cement (OPC) was used as the binding material in all mortar specimens. The chemical composition of the OPC is shown in Table 1. The aggregates were acquired from Xiamen ISO Standard Sand Co., Ltd., with particle diameters ranging from 0.5 to 2.0 mm. Iso-octyltriethoxysilane was acquired from Wacker Chemicals. Tap water was used in the preparation of mortar samples. Anhydrous ethanol was acquired from Cormio Inc, China. To ensure permeability, iso-octyltriethoxysilane was used as a low surface energy material for surface treatment with a concentration of 2%, with the remainder composed of ethanol (28%) and water (70%).

2.2. Preparation. The proportions used to prepare the mortar samples and their properties after 28 days of curing are shown in Table 2. To ensure the uniformity of all mortar blocks, the following mixing process was adopted: (1) 450 g of cement and 225 g of water were added to the mixer and stirred for 60 s at slow speed; (2) 1350 g of sand was added evenly for 30 s; (3) the mixture was stirred at high speed for 30 s; (4) the mixer was stopped for 90 s for manual mixing; and (5) the mixture was further stirred for 60 s at high speed. After the concrete mixture was mixed, it was horizontally poured into a cuboid mold (40 mm × 40 mm × 160 mm) and a cubic mold (40 mm × 40 mm × 40 mm). After molding, all specimens were wet cured for 24 h (RH = 100% and $T = 21 \pm 1^\circ\text{C}$) and then demolded and cured for 28 days in water ($21 \pm 1^\circ\text{C}$). The cuboid specimen was used for the FTC test, and the cubic specimen was used for water absorption and wear resistance tests.

To ensure the effective penetration of modifiers, the hydrophobic coating on the surface of the mortar specimen was prepared using an osmosis vacuum degassing device (Figure 1). After curing for 28 days, the sample was dried to a constant weight and placed in the vacuum tank. When the vacuum was below 20 kPa, the iso-octyltriethoxysilane solution was slowly infused into the vacuum tank until it inundated the entire sample. Then, the hydrophobic coating was applied to the mortar surface after drying at 60°C for 12 h.

2.3. Test Methods. The WCA was measured using a contact angle tester (KRUSS, K100, Germany). It was determined using deionized water (2.5 μL deposited with a micropipette) and by calculating the average of three measured values on the surface.

The capillary water absorption test was used to quantify the ability of the concrete to absorb water by capillary suction. To evaluate the hydrophobicity, the baseline samples and hydrophobic samples were placed in water under atmospheric pressure (101 kPa) and vacuum (20 kPa) for two days each. The weights of the samples were recorded before and after immersion to calculate the mass uptake of water. An MPD-2 metallographic polisher (Shanghai Zhongyan Instrument Co., Ltd., China) was used to determine the wear resistance of the mortar. As the polisher rotates, the sandpaper begins to slide and creates friction with the surface of the sample under pressure, such that the microstructure of the sample surface will be destroyed. After polishing, the mass loss rate was calculated and the mass uptake of water was measured. 240-grit sandpaper was fixed on the turntable of the polisher, and the turntable rotated at 500 rpm. The longer the polishing time, the higher the wear degree of the test block. In this study, the lengths of polished mortar blocks indicate the degree of wear.

The KDR-A rapid freeze-thaw circulator (Beijing Kangluda Test Instrument Co., Ltd., China) was used to determine the FTC resistance (Figure 2). The sample was immersed in water for two days and then put into the rubber sleeve of the circulator, which was filled with water. The temperature cycle consisted of freezing and heating stages

TABLE 1: Chemical composition of ordinary Portland cement (P. O42.5R).

	Chemical composition (%)									
	SiO ₂	Al ₂ O ₃	CaO	Fe ₂ O ₃	MgO	K ₂ O	TiO ₂	Na ₂ O	SO ₃	Others
Cement	19.26	4.33	65.46	3.06	1.60	0.77	—	0.13	4.45	0.94

TABLE 2: Mix proportions and mechanical properties of the mortar.

Water-cement ratio	Raw material (g)			Density (kg/m ³)	Mechanical parameter at 28 d (MPa)	
	Cement	Water	Sand		Compressive strength	Flexural strength
0.5	450	225	1350	2300	52.4	12.8

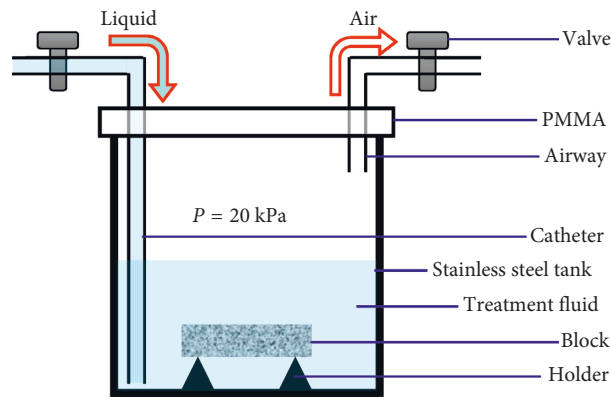


FIGURE 1: Schematic of osmosis vacuum degassing device.

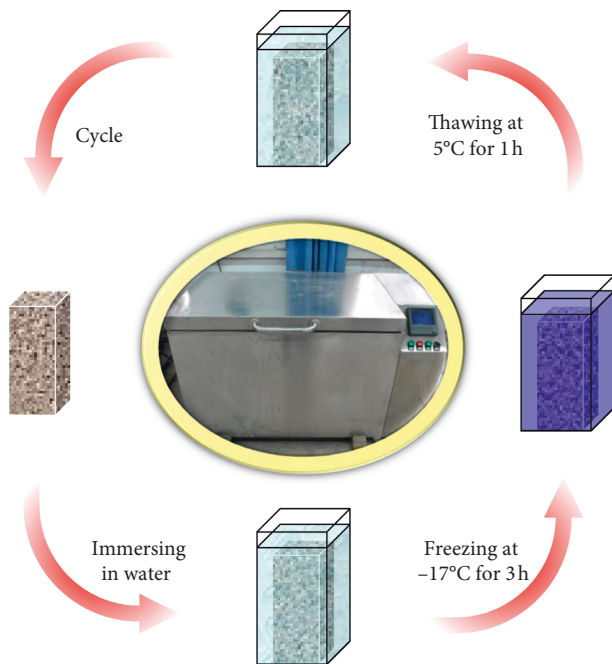


FIGURE 2: Schematic of the freeze-thaw cycle (FTC) test.

and took approximately four hours in total. During the freezing stage, the water temperature dropped from 5°C to -17°C after 2.5 h. During the melting stage, the water temperature rose from -17°C to 5°C after 1.5 h. With an

increase in the FTCs, the damage degree of the samples increased. After FTC damage, the mass loss rates and flexural and compressive strengths of the samples were measured to evaluate their degrees of damage.

The microscopic morphologies of the samples were observed by SEM (MAIA3, TESCAN, Czech Republic). Fourier transform infrared spectroscopy (FT-IR) spectra were acquired in the range of 400–4000 cm⁻¹ with an IR spectrophotometer (380FTIR, Thermo Fisher Scientific, America). The flexural and compressive strengths of the mortar were evaluated on the same testing machine (SANS CMT5105, Shenzhen, China) at a loading rate of 2400 ± 200 N/s.

3. Results and Discussion

3.1. Wetting Properties and Water Contact Angle. Without changing the surface microstructures of the mortar specimens, the surface of the mortar shows good hydrophobicity only through iso-octyltriethoxysilane solution modification, as shown in Figure 3(b). This phenomenon can be explained by the Wenzel theory that a hydrophobic surface can be obtained by modifying the rough mortar sample with low surface energy materials. First, iso-octyltriethoxysilane is hydrated to produce silanols (Si-OH). Secondly, silanol is combined with quartz sand, hydrated C-S-H gel, ettringite, and calcium hydroxide through -OH group reactions. Finally, the two -OH groups of iso-octyltriethoxysilane form Si-O-Si bonds by condensation while

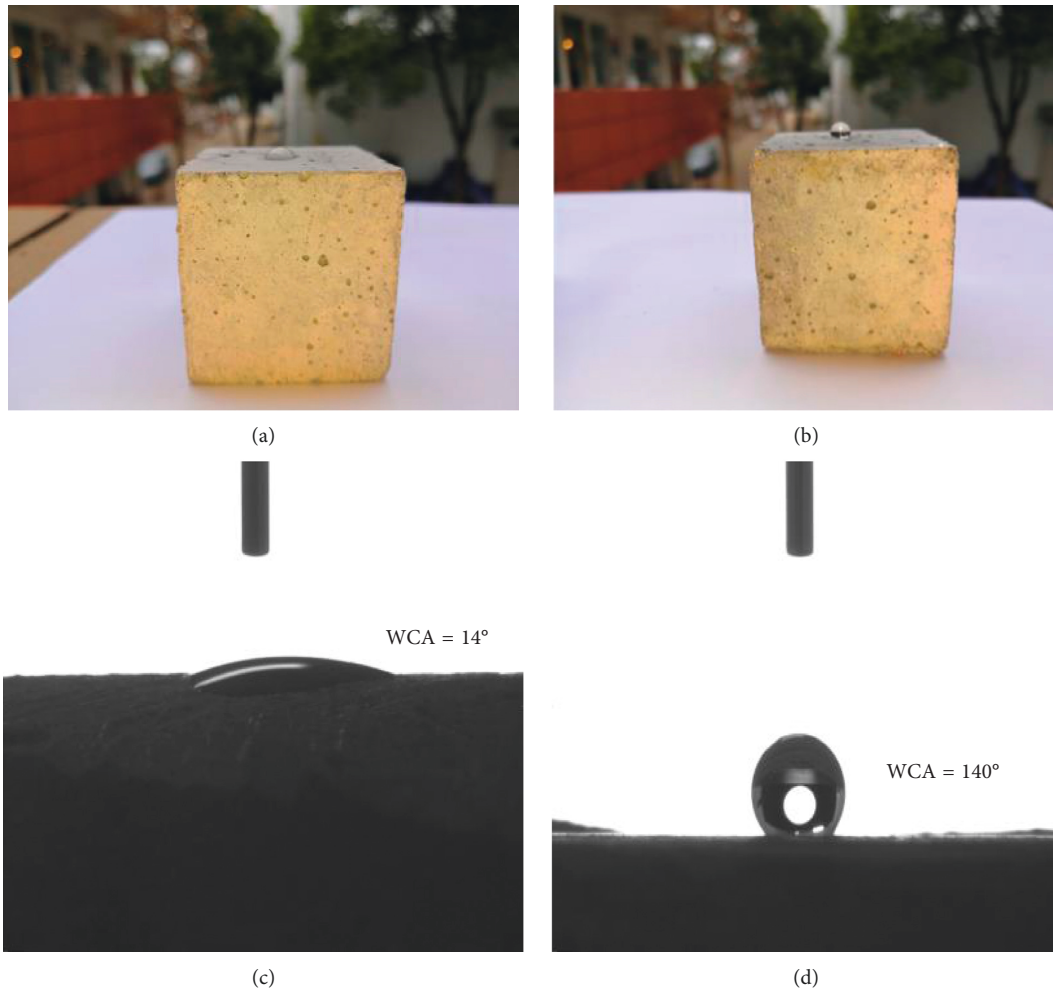


FIGURE 3: Water contact angles on the surface of mortar specimens: (a) baseline sample, (b) hydrophobic sample, (c) WCA of the baseline sample, and (d) WCA of the hydrophobic sample.

releasing water. After the above reaction, iso-octyltriethoxysilane forms a continuous self-assembled molecular film on the surface of the hydrated products. Iso-octyltriethoxysilane contains a $-\text{CH}_3$ group and $-\text{CH}_2$ group which effectively reduce the surface energy of the cement mortar. Therefore, the rough surface structure modified by low surface energy materials exhibits excellent hydrophobic properties.

Figure 3(c) shows that the contact angle of the baseline sample is approximately 14° , indicating that the porous, rough surface of the mortar belongs to the hydrophilic surface. Figure 3(d) shows that the WCA of the modified mortar surface increases to 140° , which proves that a hydrophobic surface can be obtained by modifying the rough hydrophilic surface with low surface energy materials. The WCA of the modified mortar surface did not reach a super-hydrophobic state ($\theta > 150$) because the surface roughness of the mortar itself did not conform to the Cassie–Baxter model. The fragile micro/nanostructure is not conducive to the wear resistance of the coating itself. Therefore, the obtained WCA ($\theta = 140^\circ$) is sufficient to improve the waterproof performance of the mortar.

3.2. Water Absorption. The influence of the hydrophobic coating on the water absorption of the mortar samples is shown in Figure 4. The results show that the cumulative water uptake of the baseline sample increased gradually from the beginning to achieve equilibrium and remained at a stable level thereafter, while the water absorption of the hydrophobic sample remained at a low level. After 15 days of immersion, the cumulative water uptake of the hydrophobic samples was reduced by 90%. This excellent waterproofing effect is equivalent to the waterproofing effect of a nano-composite waterproof coating [45].

The microscale rough structure of the mortar surface is modified by the low surface energy material to reach a Wenzel state, which shows an excellent waterproofing effect. The unmodified samples retain the hydrophilic properties of the cement-based materials.

3.3. Wear Resistance and Thickness of the Hydrophobic Coating. Fragile micro/nanostructures on hydrophobic surfaces are susceptible to damage, leading to degradation of the hydrophobic properties. In this research, to test the wear resistance of the hydrophobic coating, the mortar sample

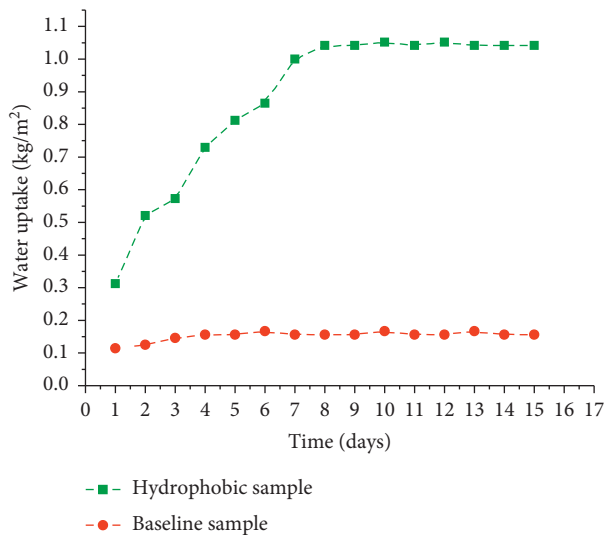


FIGURE 4: Water absorption results for the baseline and hydrophobic samples.

was placed on a burnisher and polished with 240-grit sandpaper at 500 rpm, and then the water absorption was tested. The lengths of the mortar blocks after polishing indicate their degrees of wear. Table 3 lists the length reductions corresponding to different polishing times.

As shown in Figure 5(c), after polishing, the WCA ($\theta = 77^\circ$) of sample 5 decreased but remained between that of the baseline sample as shown in Figure 5(a) and that of the unpolished hydrophobic sample as shown in Figure 5(b). Because the thickness of the chemically modified mortar reaches the range of 1–3 mm, the hydrophobic sample remains hydrophobic even after the rough surface structure is destroyed. In the next section, the mass loss and water absorption after polishing are discussed. Figure 6(f) shows that the mass loss rate of the samples increases with an increase in length reduction. The mass loss rate of the sample is the largest, and its WCA ($\theta = 77^\circ$) is still significant. Samples 1, 3, and 5 were immersed in water for 15 days with the baseline sample (Figure 6(a)) and the unpolished hydrophobic sample (Figure 6(b)). When the samples were immersed in water, many bubbles were observed on the surface of the baseline sample (Figure 6(a)). In contrast, we could see only a few bubbles on the surface of the hydrophobic sample (Figure 6(b)), even if it was reduced by over 10 mm by the sandpaper (Figure 6(e)). Surface bubbles are formed when water enters the sample and displaces air from the sample. A few bubbles on the surfaces of the polished samples show that the hydrophobic coating maintains an excellent waterproofing performance even after polishing. In the cumulative water uptake test, it was also proved that the hydrophobic coatings have excellent wear resistance, as shown in Figure 7.

In Figure 7, the water absorption curve shows that the cumulative water uptake of the polished hydrophobic samples remained at a low level. This phenomenon shows that the wear resistance of the hydrophobic coating is outstanding. The surface of the hydrophobic coating is worn after polishing, which leads to decreased WCA, but it still

maintains excellent waterproof properties. This phenomenon can be explained by Figure 8.

Figure 8 illustrates the thickness of the hydrophobic coating by wetting the cross section with water. In this figure, the light hydrophobic coating can be observed continuously around the perimeter of the dark central area, which indicates that a continuous hydrophobic coating was formed on the surface of the sample by vacuum impregnation. The thickness of the hydrophobic coating is within the range of 1–3 mm. This is a reasonable explanation for the hydrophobic properties of the polished hydrophobic samples decreasing after polishing but the waterproof properties remaining excellent. When iso-octyltriethoxysilane penetrates the mortar sample, self-assembled membranes will form on the surface of the hydrated particles. As the interior of the mortar is rough and porous, a stable hydrophobic network structure with a certain thickness is obtained. In this way, even if the surface of the microscale rough structure is destroyed, the network structure can still play a perfect waterproofing role.

3.4. FTC Resistance Analysis. As shown in Figure 9, steep curves for the mass loss rate and flexural and compressive strengths were observed for the baseline sample after the FTC tests. On the contrary, the corresponding curves for the hydrophobic samples change more smoothly. This phenomenon shows that the baseline sample was severely damaged after the FTCs, while the hydrophobic sample was much less damaged due to the protection of its hydrophobic coating. After 36 FTC tests, the mass loss rate of the baseline sample was approximately 48.0 wt.%. Meanwhile, the flexural and compressive strengths of the baseline sample were reduced to 0.3 MPa and 11.0 MPa, respectively. After 36 FTC tests, the mass loss rate and flexural and compressive strengths of the hydrophobic sample were 0.8 wt.%, 7.5 MPa, and 38.2 MPa, respectively. After 48 FTC tests, the baseline sample lost its original morphology and size (Figure 10) because its mass loss rate was over 62 wt.%. In contrast, the original morphology and size of the hydrophobic sample remained after 72 FTC tests (Figure 10). The test results show that the mass loss rate and flexural and compressive strengths of the hydrophobic sample are 10.4 wt.%, 1.0 MPa, and 16.5 MPa, respectively, which are very close to the values of the baseline sample after 24 FTCs. The test results indicate that the hydrophobic coating not only has an excellent waterproofing effect but it also has excellent anti-FTC performance. Due to the protective effect of the hydrophobic coating, water cannot impregnate the sample, thus alleviating damage from FTCs. Exfoliation of the surface coating of the hydrophobic sample occurred at the 36th cycle. This is because the sample had been immersed in water at below 0°C . The sample was encapsulated by external ice, which produced certain stresses and destroyed the hydrophobic coating. It is predicted that increasing the hydrophobic coating thickness will effectively improve the FTC resistance of the samples. This will be further explored in future research. The improvement of frost resistance was also observed in concrete modified with metakaolin and

TABLE 3: Length reduction of the modified sample.

Sample number	Radius of turntable (mm)	Burnisher revolutions per minute	Polish time (min)	Polish distance (km)
1			0.5	0.3
2			4.5	2.8
3	100	500	8.5	5.4
4			12.5	7.9
5			16.6	10.4

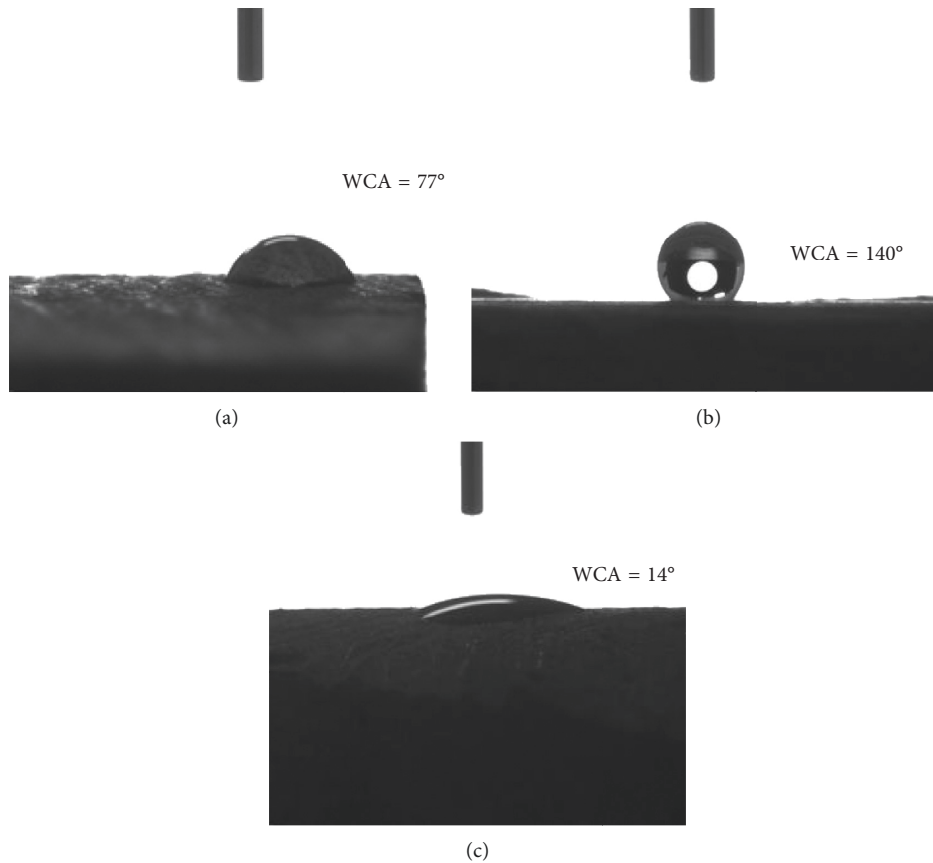


FIGURE 5: WCA of the (a) baseline sample, (b) hydrophobic sample, and (c) polished hydrophobic sample.

nanoparticles [46]. This is an entirely different technical concept from the hydrophobic coating, but it can be combined to achieve better frost resistance in future research.

3.5. Microscopic Analysis and Chemical Characterization.

To study the effect of the FTC on the internal structure of the mortar, the sectional microstructures of the hydrophobic and the samples were compared after enduring FTC damage (Figure 11). As shown in Figure 11(a), after the 12th FTC test, a visible crack could be seen on the baseline sample. Moreover, the crack was further extended due to the continuous damage from FTC after the 36th FTC test. The width of the crack increased from 2.1 μm to 4.3 μm (Figure 12(b)). Significantly, only cracks less than 1 μm (Figure 11(c)) could be observed on the hydrophobic sample after the 12th FTC test. After the 48th

FTC test, a crack becomes evident with a width of approximately 1 μm (Figure 11(d)). As exhibited in Figure 11(e), the width of the crack is still below 4 μm after the 72nd FTC test. Figure 11(f) displays the microstructure of the hydrophobic coating on the mortar block after enduring 72 FTCs, indicating that the hydrophobic coating could effectively reduce the damage to the mortar caused by FTCs. Based on this, we can confidently predict that the FTC resistance of the mortar block would be improved by increasing the thickness of the hydrophobic coating.

As shown in Figure 12(a), the hydrophobic coating appeared after the sample section was wet with water. In Figure 12(b), by magnifying by 20,000 times, the SEM images show that the interior of the mortar is filled with acicular or flaky hydration products. This micron-scale rough structure is one of the conditions for the formation of the hydrophobic coating. The chemical modification of the

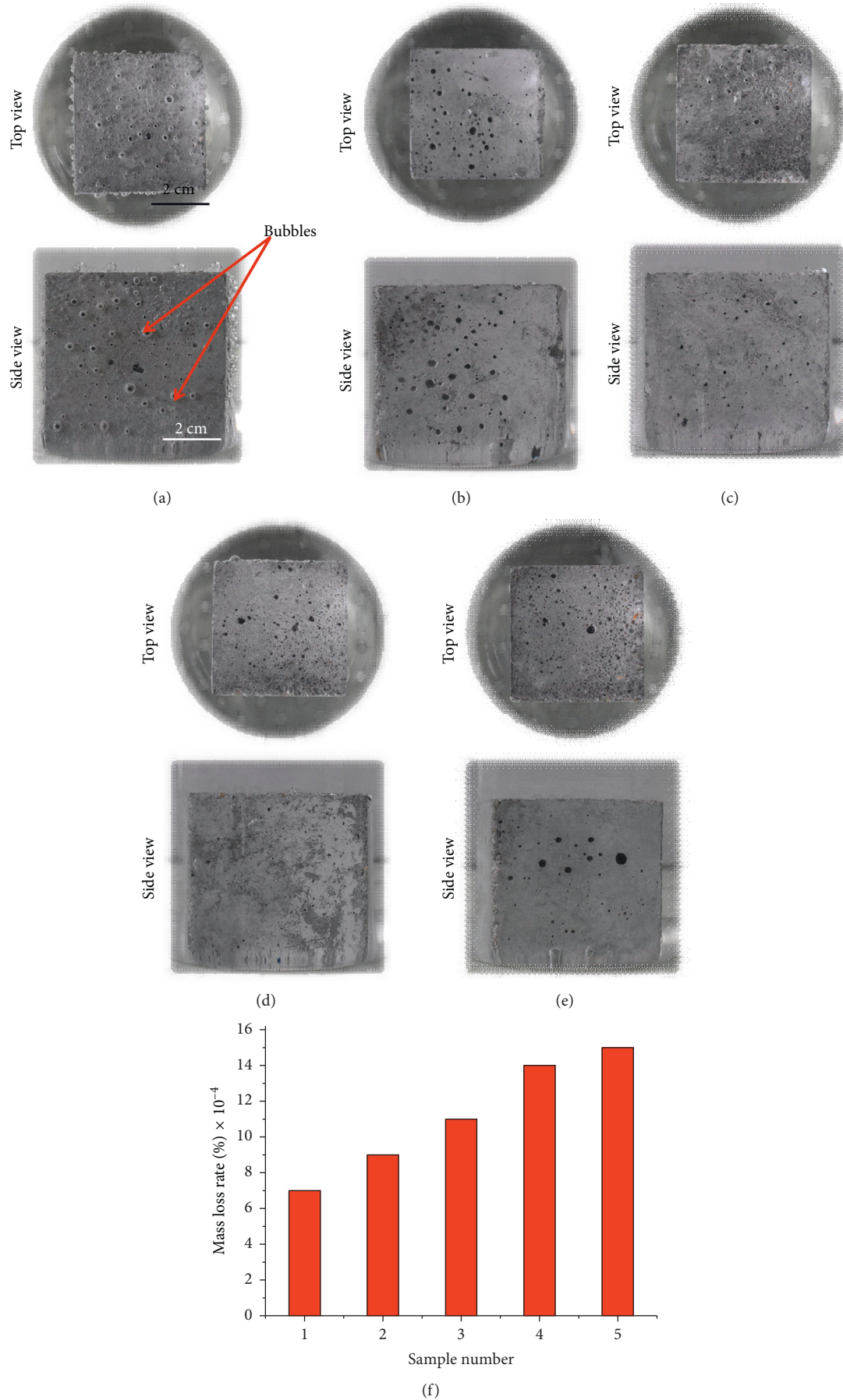


FIGURE 6: Photograph of the mortar block immersed in water: (a) contrast sample and (b) hydrophobic sample and after abrasion with 240-grit sandpaper for (c) 0.3 mm, (d) 5.3 mm, and (e) 10.4 km. (f) Mass loss rate after polishing.

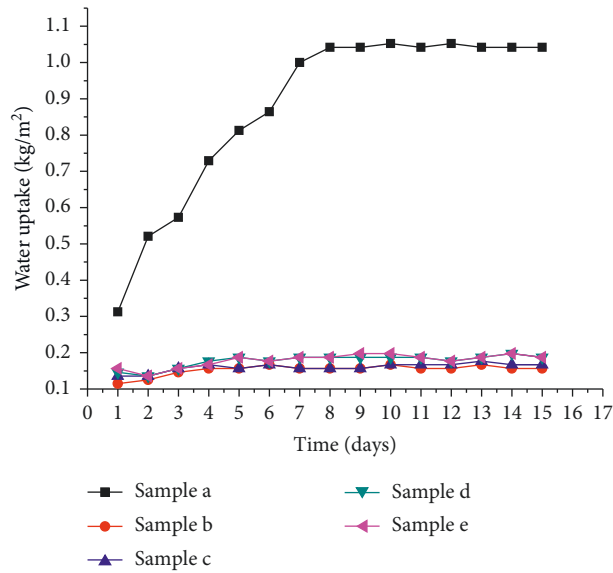


FIGURE 7: Effect of length reduction on water absorption of the hydrophobic sample.

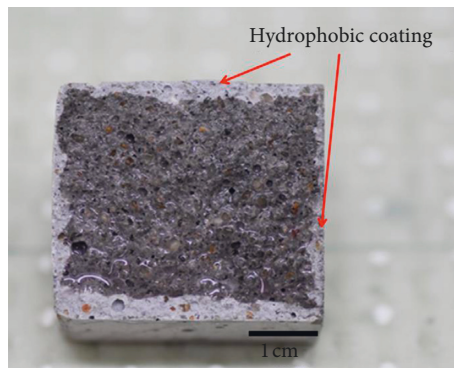


FIGURE 8: Photograph of the hydrophobic coating's thickness.

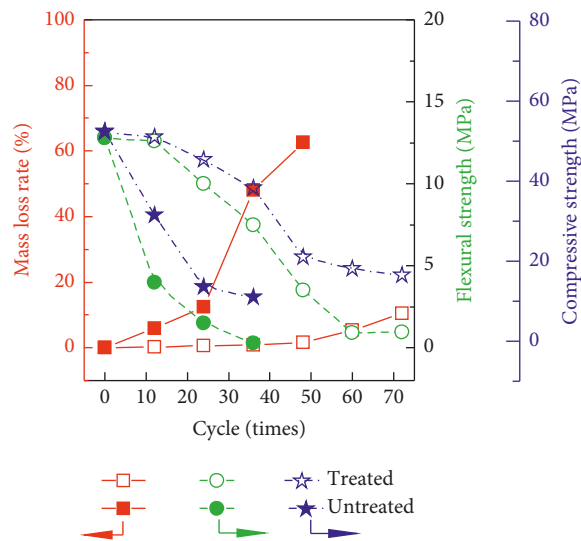


FIGURE 9: Mass loss rate (■ and □) and flexural (● and ○) and compressive (★ and ☆) strengths of the hydrophobic sample (□, ○, and ☆) and baseline sample (■, ●, and ★) measured after FTC tests.

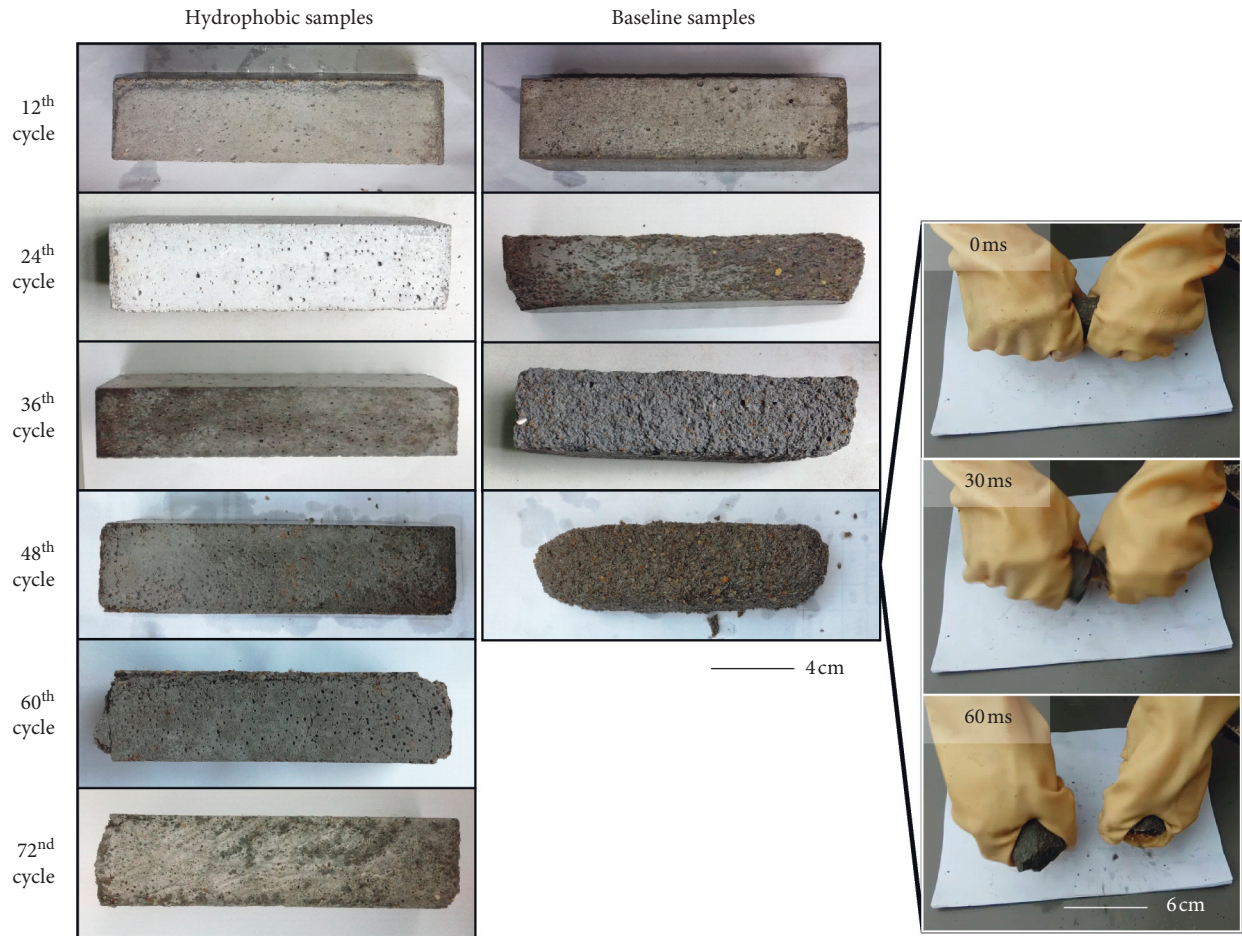


FIGURE 10: Photographs of the sample after different FTC tests.

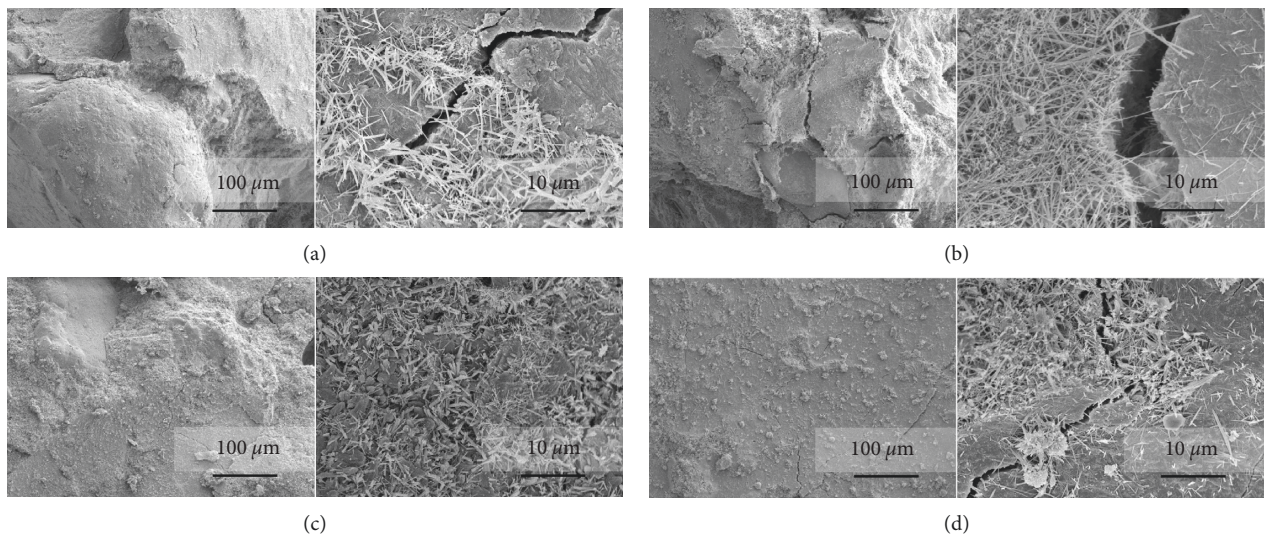


FIGURE 11: Continued.

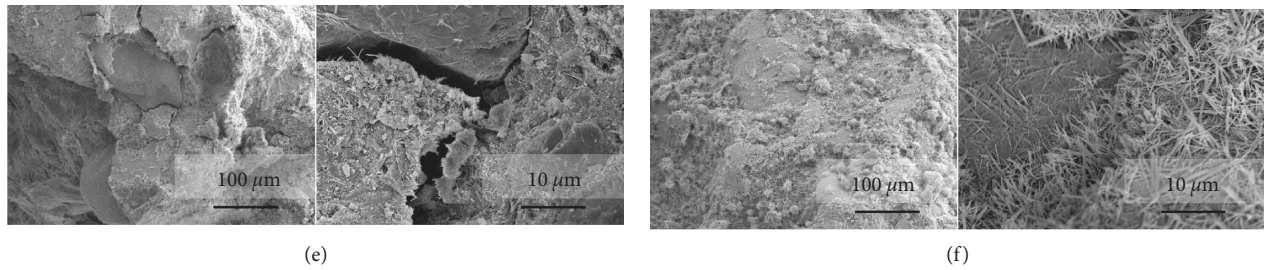


FIGURE 11: Micrographs of the mortar sample. Sectional microstructure of the baseline sample at the (a) 12th and (b) 36th FTCs. Sectional microstructure of the hydrophobic sample at the (c) 12th, (d) 36th, and (e) 72nd FTCs. (f) Microstructure of the hydrophobic coating on the hydrophobic sample at the 72nd FTC.

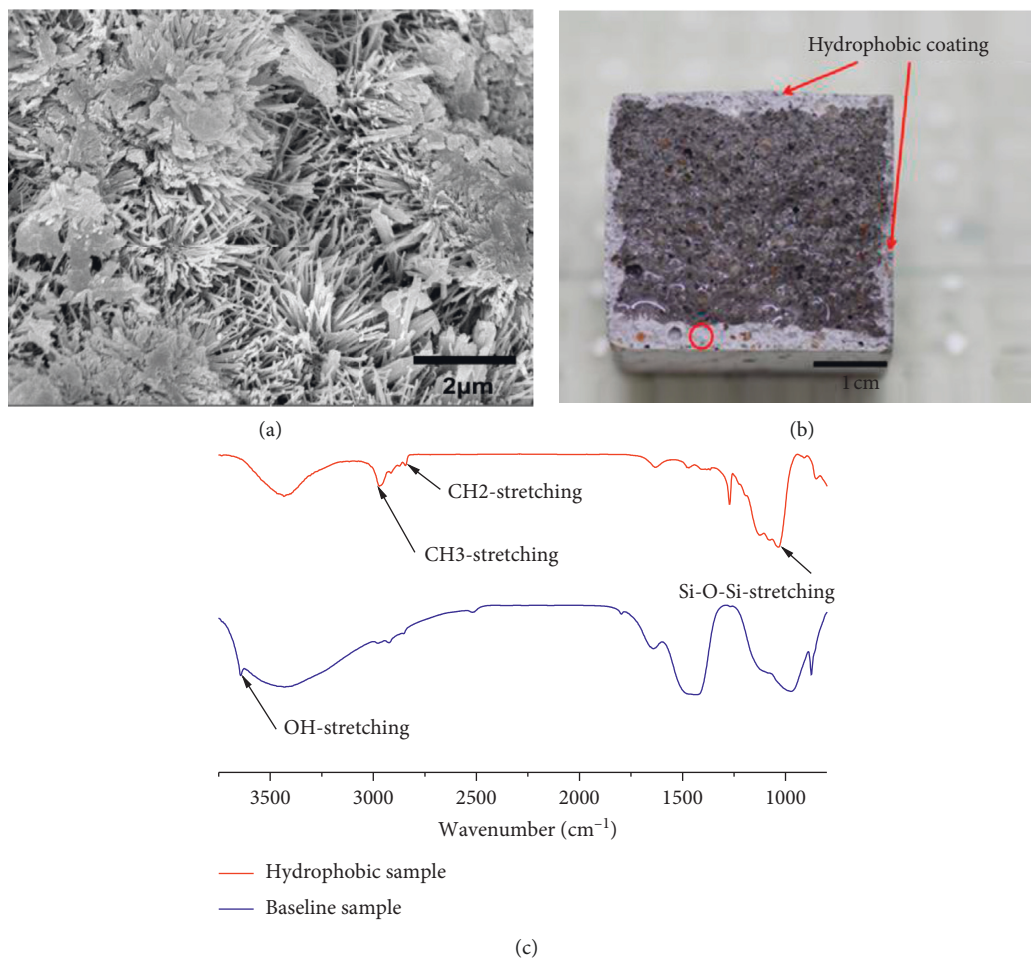


FIGURE 12: Microscopic analysis and chemical characterization of the hydrophobic coating: (a) hydrophobic sample, (b) SEM photograph of the hydrophobic coating, and (c) FT-IR spectra of the sample.

hydration products was characterized by the FT-IR. As shown in Figure 12(c), the FT-IR wavenumbers ranged from 3750 cm^{-1} to 1000 cm^{-1} . The absorption peak at 3644 cm^{-1} was attributed to the stretching vibration of $-\text{OH}$ from $\text{Ca}(\text{OH})_2$. The $-\text{OH}$ stretching vibration peaks of $\text{Ca}(\text{OH})_2$ were only observed in the baseline sample. This indicates that hydroxyl groups are consumed in the reaction of calcium hydroxide with iso-octyltriethoxysilane. Absorption peaks at

2970 cm^{-1} and 2920 cm^{-1} were observed in the hydrophobic coating, corresponding to $-\text{CH}_3$ and $-\text{CH}_2$ groups, respectively, implying that chemical bonds are formed between the coating and cement hydration products. The hydrophobic coating peak at 1130 cm^{-1} corresponds to the Si-O-Si group, which shows that continuous self-assembled molecular films are formed on the surface of hydration products.

4. Conclusions

This study aimed to transform a porous, hydrophilic cement mortar surface into a hydrophobic surface by chemical modification. Through hydrolysis and condensation, iso-octyltriethoxysilane forms continuous self-assembled molecular films on the surface of hydrated products, thus producing a hydrophobic coating with a thickness of 1–3 mm on the surface of the mortar. The WCA of the hydrophobic coating was 140°, and it had good waterproofing and wear resistance. A water absorption test showed that the cumulative water uptake of the hydrophobic samples decreased by 90%. Compared with a baseline sample, the mass loss rate and flexural and compressive strengths of the hydrophobic sample increased several-fold in the FTC test stages. Chemical bonding between iso-octyltriethoxysilane and cement hydration products ensures excellent wear resistance of the hydrophobic coating. In conclusion, the hydrophobic coating prepared by vacuum impregnation has an excellent protective effect on cement-based materials, and this technology has a wide range of applications in the building industry. Future work will focus on the preparation of hydrophobic coatings with higher thicknesses and better waterproofing performances via a simpler process.

Data Availability

All the data in this study are original.

Conflicts of Interest

The authors declare that they have no conflicts of interest.

Acknowledgments

This work was supported by the National Key R&D Plan (grant no. 2016YFC0701004), the Sichuan Science and Technology Program (no. 2019ZDZX0024), and the Doctoral Research Foundation of Southwest University of Science and Technology (18zx7134).

References

- [1] N. R. Rakhimova, R. Z. Rakhimov, Y. N. Osin et al., “Solidification of nitrate solutions with alkali-activated slag and slag-metakaolin cements,” *Journal of Nuclear Materials*, vol. 457, pp. 186–195, 2015.
- [2] S. Chatterji, “Aspects of the freezing process in a porous material-water system,” *Cement and Concrete Research*, vol. 29, no. 4, pp. 627–630, 1999.
- [3] M. J. Setzer, “Mechanical stability criterion, triple-phase condition, and pressure differences of matter condensed in a porous matrix,” *Journal of Colloid and Interface Science*, vol. 235, no. 1, pp. 170–182, 2001.
- [4] L. Liu, S. Wu, H. Chen, and Z. Haitao, “Numerical investigation of the effects of freezing on micro-internal damage and macro-mechanical properties of cement pastes,” *Cold Regions Science and Technology*, vol. 106–107, pp. 141–152, 2014.
- [5] M. K. Ismail and A. A. A. Hassan, “Abrasion and impact resistance of concrete before and after exposure to freezing and thawing cycles,” *Construction and Building Materials*, vol. 215, pp. 849–861, 2019.
- [6] S. Pilehvar, A. M. Szczotok, J. F. Rodríguez et al., “Effect of freeze-thaw cycles on the mechanical behavior of geopolymer concrete and portland cement concrete containing micro-encapsulated phase change materials,” *Construction and Building Materials*, vol. 200, pp. 94–103, 2019.
- [7] H.-S. Shang and T.-H. Yi, “Freeze-thaw durability of air-entrained concrete,” *Scientific World Journal*, vol. 2013, Article ID 650791, 6 pages, 2013.
- [8] S. Jin, J. Zhang, and B. Huang, “Fractal analysis of effect of air void on freeze-thaw resistance of concrete,” *Construction and Building Materials*, vol. 47, pp. 126–130, 2013.
- [9] W. Micah Hale, S. F. Freyne, and B. W. Russell, “Examining the frost resistance of high performance concrete,” *Construction and Building Materials*, vol. 23, no. 2, pp. 878–888, 2009.
- [10] R. Zhao, Y. Yuan, Z. Cheng et al., “Freeze-thaw resistance of class F fly ash-based geopolymer concrete,” *Construction and Building Materials*, vol. 222, pp. 474–483, 2019.
- [11] F. U. A. Shaikh and S. W. M. Supit, “Compressive strength and durability properties of high volume fly ash (HVFA) concretes containing ultrafine fly ash (UFFA),” *Construction and Building Materials*, vol. 82, pp. 192–205, 2015.
- [12] A. Salas, S. Delvasto, R. M. de Gutierrez, and D. Lange, “Comparison of two processes for treating rice husk ash for use in high performance concrete,” *Cement and Concrete Research*, vol. 39, no. 9, pp. 773–778, 2009.
- [13] J. Nam, G. Kim, B. Lee, R. Hasegawa, and Y. Hama, “Frost resistance of polyvinyl alcohol fiber and polypropylene fiber reinforced cementitious composites under freeze thaw cycling,” *Composites Part B: Engineering*, vol. 90, pp. 241–250, 2016.
- [14] S. N. Pogorelov and G. S. Semenyak, “Frost resistance of the steel fiber reinforced concrete containing active mineral additives,” *Procedia Engineering*, vol. 150, pp. 1491–1495, 2016.
- [15] I. Vegas, J. J. Gaitero, J. Urreta, R. García, and M. Frías, “Aging and durability of ternary cements containing fly ash and activated paper sludge,” *Construction and Building Materials*, vol. 52, pp. 253–260, 2014.
- [16] M. I. Khan and R. Siddique, “Utilization of silica fume in concrete: review of durability properties,” *Resources, Conservation and Recycling*, vol. 57, pp. 30–35, 2011.
- [17] B. B. Sabir, “Mechanical properties and frost resistance of silica fume concrete,” *Cement and Concrete Composites*, vol. 19, no. 4, pp. 285–294, 1997.
- [18] P. Zhang and Q.-f. Li, “Effect of silica fume on durability of concrete composites containing fly ash,” *Science and Engineering of Composite Materials*, vol. 20, no. 1, pp. 57–65, 2013.
- [19] H.-S. Kim, S.-H. Lee, and H.-Y. Moon, “Strength properties and durability aspects of high strength concrete using Korean metakaolin,” *Construction and Building Materials*, vol. 21, no. 6, pp. 1229–1237, 2007.
- [20] P. Duan, Z. Shui, W. Chen, and C. Shen, “Enhancing microstructure and durability of concrete from ground granulated blast furnace slag and metakaolin as cement replacement materials,” *Journal of Materials Research and Technology*, vol. 2, no. 1, pp. 52–59, 2013.
- [21] P. Reiterman, O. Holčapek, O. Zobal, and M. Keppert, “Freeze-thaw resistance of cement screed with various supplementary cementitious materials,” *Reviews on Advanced Materials Science*, vol. 58, no. 1, pp. 66–74, 2019.
- [22] F. B. P. D. Costa, D. P. Righi, A. G. Graeff, and L. C. P. d. Silva Filho, “Experimental study of some durability properties of

- ECC with a more environmentally sustainable rice husk ash and high tenacity polypropylene fibers,” *Construction and Building Materials*, vol. 213, pp. 505–513, 2019.
- [23] C.-S. Shon, A. Abdigaliyev, S. Bagitova, C.-W. Chung, and D. Kim, “Determination of air-void system and modified frost resistance number for freeze-thaw resistance evaluation of ternary blended concrete made of ordinary portland cement/silica fume/class F fly ash,” *Cold Regions Science and Technology*, vol. 155, pp. 127–136, 2018.
- [24] A. S. Gill and R. Siddique, “Strength and micro-structural properties of self-compacting concrete containing metakaolin and rice husk ash,” *Construction and Building Materials*, vol. 157, pp. 51–64, 2017.
- [25] L. Feng, S. Li, Y. Li et al., “Super-hydrophobic surfaces: from natural to artificial,” *Advanced Materials*, vol. 14, no. 24, pp. 1857–1860, 2002.
- [26] D. Zang, R. Zhu, W. Zhang et al., “Corrosion-resistant superhydrophobic coatings on Mg alloy surfaces inspired by Lotus seedpod,” *Advanced Functional Materials*, vol. 27, no. 8, pp. 1–7, 2017.
- [27] X. Gao, X. Yan, X. Yao et al., “The dry-style antifogging properties of mosquito compound eyes and artificial analogues prepared by soft lithography,” *Advanced Materials*, vol. 19, no. 17, pp. 2213–2217, 2007.
- [28] X. Gao and L. Jiang, “Biophysics: water-repellent legs of water striders,” *Nature*, vol. 432, no. 7013, p. 36, 2004.
- [29] S. Mokhtari, F. Karimzadeh, M. H. Abbasi, and K. Raeissi, “Development of super-hydrophobic surface on Al 6061 by anodizing and the evaluation of its corrosion behavior,” *Surface and Coatings Technology*, vol. 324, pp. 99–105, 2017.
- [30] Y. Gao, L. Qu, B. He, K. Dai, Z. Fang, and R. Zhu, “Study on effectiveness of anti-icing and deicing performance of super-hydrophobic asphalt concrete,” *Construction and Building Materials*, vol. 191, pp. 270–280, 2018.
- [31] C.-W. Lin, C.-J. Chung, C.-M. Chou, and J.-L. He, “Morphological effect governed by sandblasting and anodic surface reforming on the super-hydrophobicity of AISI 304 stainless steel,” *Thin Solid Films*, vol. 620, pp. 88–93, 2016.
- [32] E. M. Elnaggar, T. M. Elsokkary, M. A. Shohide, B. A. El-Sabbagh, and H. A. Abdel-Gawwad, “Surface protection of concrete by new protective coating,” *Construction and Building Materials*, vol. 220, pp. 245–252, 2019.
- [33] R. N. Wenzel, “Resistance of solid surfaces to wetting by water,” *Industrial & Engineering Chemistry*, vol. 28, no. 8, pp. 988–994, 1936.
- [34] W. She, X. Wang, C. Miao et al., “Biomimetic super-hydrophobic surface of concrete: topographic and chemical modification assembly by direct spray,” *Construction and Building Materials*, vol. 181, pp. 347–357, 2018.
- [35] F. Tittarelli and G. Moriconi, “Comparison between surface and bulk hydrophobic treatment against corrosion of galvanized reinforcing steel in concrete,” *Cement and Concrete Research*, vol. 41, no. 6, pp. 609–614, 2011.
- [36] I. Flores-Vivian, V. Hejazi, M. I. Kozhukhova, M. Nosonovsky, and K. Sobolev, “Self-assembling particle-siloxane coatings for superhydrophobic concrete,” *ACS Applied Materials & Interfaces*, vol. 5, no. 24, pp. 13284–13294, 2013.
- [37] Z. Liu and W. Hansen, “Effect of hydrophobic surface treatment on freeze-thaw durability of concrete,” *Cement and Concrete Composites*, vol. 69, pp. 49–60, 2016.
- [38] Z. Song, X. Xue, Y. Li et al., “Experimental exploration of the waterproofing mechanism of inorganic sodium silicate-based concrete sealers,” *Construction and Building Materials*, vol. 104, pp. 276–283, 2016.
- [39] S. Weisheit, S. H. Unterberger, T. Bader, and R. Lackner, “Assessment of test methods for characterizing the hydrophobic nature of surface-treated high performance concrete,” *Construction and Building Materials*, vol. 110, pp. 145–153, 2016.
- [40] H. Herb, A. Gerdes, and G. Brenner-Weiß, “Characterization of silane-based hydrophobic admixtures in concrete using TOF-MS,” *Cement and Concrete Research*, vol. 70, pp. 77–82, 2015.
- [41] A. Arabzadeh, H. Ceylan, S. Kim et al., “Superhydrophobic coatings on portland cement concrete surfaces,” *Construction and Building Materials*, vol. 141, pp. 393–401, 2017.
- [42] H. Husni, M. R. Nazari, H. M. Yee et al., “Superhydrophobic rice husk ash coating on concrete,” *Construction and Building Materials*, vol. 144, pp. 385–391, 2017.
- [43] H. S. Wong, R. Barakat, A. Alhilali, M. Saleh, and C. R. Cheeseman, “Hydrophobic concrete using waste paper sludge ash,” *Cement and Concrete Research*, vol. 70, pp. 9–20, 2015.
- [44] M. Horgnies and J. J. Chen, “Superhydrophobic concrete surfaces with integrated microtexture,” *Cement and Concrete Composites*, vol. 52, pp. 81–90, 2014.
- [45] P. Scarfato, L. Di Maio, M. L. Fariello, P. Russo, and L. Incarnato, “Preparation and evaluation of polymer/clay nanocomposite surface treatments for concrete durability enhancement,” *Cement and Concrete Composites*, vol. 34, no. 3, pp. 297–305, 2012.
- [46] P. Reiterman, “Influence of metakaolin additive and nanoparticle surface treatment on the durability of white cement based concrete,” *European Journal of Environmental and Civil Engineering*, pp. 1–14, 2018.

Research Article

Slurry and Technology Optimization for Grouting Fissures in Earthen Sites with Quicklime

Kai Cui ^{1,2}, Fei Feng ¹, Wen-wu Chen ², Dong-hua Wang ¹ and Xiao-hai Wang ¹

¹Engineering Research Center of Ministry of Education for Disaster Prevention and Mitigation of Civil Engineering in Western China, Lanzhou University of Technology, Lanzhou 730050, China

²Key Laboratory of Mechanics on Disaster and Environment in Western China, Lanzhou University, Ministry of Education, Lanzhou 730000, China

Correspondence should be addressed to Fei Feng; 824290056@qq.com

Received 13 December 2018; Revised 11 April 2019; Accepted 22 April 2019; Published 9 May 2019

Guest Editor: Alexandra Rempel

Copyright © 2019 Kai Cui et al. This is an open access article distributed under the Creative Commons Attribution License, which permits unrestricted use, distribution, and reproduction in any medium, provided the original work is properly cited.

Shrinkage differentiation and the need for multiple replenishments of slurry after fissure reinforcement are key problems for the grouting reinforcement of fissures in earthen sites. In this study, quicklime was mixed with 1.5% SH binder, clay, and fly ash in different proportions to prepare nine different mixtures and water-cement ratios of SH-(CaO + C + F) slurry. An expansibility test was performed, and based on the results, four groups of slurry were selected for a fluidity test. Ultimately, three different water-cement ratios were considered, and the mixing ratio of 3 : 2 : 5 was determined to produce the optimum slurry. The curing age was optimized according to the intensity and tensile and flexural strengths of the concretion. The selected slurry and curing age were then applied to testing traditional grouting technology and optimized grouting technology (i.e., microlime piles in the fissure) in fissure grouting field experiments. The acoustic wave, penetration resistance, and infrared thermal imaging results after fissure grouting were used to develop a preliminary explanation for the related mechanisms of slurry swelling, hardening, and lime pile compaction. The results showed that the combination of the preferred slurry and optimized grouting technology help address the problems of shrinkage differentiation on both sides of the fissure and need for multiple replenishments of the slurry after grouting.

1. Introduction

Earthen architectural sites are relics left over from production, culture, religion, and military activities in human history [1]. After hundreds of years of erosion, they have become increasingly precious because of their important historical positivism and nonrenewability [2–5]. However, in the arid areas of Northwest China, most earthen sites are exposed to adverse environmental factors for long periods of time, which results in cracking, collapse, erosion, and other damages. This poses a serious threat to the long-term preservation of earthen sites. Fissures are the most common type of damage to earthen sites and cause media discontinuities and instability [6]. Their mechanism and prevention have become the focus of research on earthen site conservation. At present, the most common treatment of fissures is grouting technology [7–9]. However, the large

shrinkage and deformation of traditional grouting slurry and the limitations of grouting technology mean that the concretion formed by the slurry easily detaches from the soil on both sides of a fissure after drying. Thus, the slurry needs to be replenished multiple times to seal the fissure. Screening candidate grouting materials and optimizing the grouting process are important for developing a slurry and grouting process that are more compatible with earthen sites in different regions.

In recent years, a consensus has developed of exploring traditional building materials and techniques to find grouting materials that are more compatible with the soil of earthen sites for conservation. Quicklime is one such traditional building material that has received a great deal of attention. Its use in China can be traced back to the Qijia cultural site in the upper reaches of the Yellow River 4000 years ago, and it has played an important role in

military, cultural, and religious construction [10, 11]. Studies have shown that quicklime has properties similar to those of European hydraulic lime [12–14], which has not only good expansion and bonding properties [15] but also good compatibility with earthen sites. It has been applied to anchoring [16] and crack grouting [17] in reinforcement projects, and good results have been achieved. At present, domestic scholars have carried out a series of modification studies on traditional lime materials [18, 19]. However, although hydraulic lime is widely used in the repair and reinforcement of historical buildings in Europe and the United States [20–22], China's application of quicklime materials to soil restoration works is still lagging.

The aim of the present study was to improve the compatibility and expansibility of the slurry. In order to fully exploit the expansibility and bonding properties of quicklime (CaO), it was mixed with fly ash (F) and crushed site soil (C) with a 1.5% SH solution as a binder to make a new SH-(CaO + F + C) slurry. The expansion ratio and fluidity index of nine sample groups with different ingredient proportions and water-cement ratios were evaluated, and three groups with good fluidity and swelling properties were selected. The three preferred groups were cured for continuous but different periods of time to form concretions. The intensity and tensile and flexural strengths of the concretions were evaluated to determine the optimum curing age. The optimized slurry was then used with both traditional grouting technology and optimized grouting technology (i.e., microlime piles in the fissure) in fissure grouting field experiments. After curing for 63 d, acoustic wave, penetration resistance, and infrared thermal imaging tests were conducted to evaluate the reinforcement. The results showed that the mixture of CaO : F : C = 3 : 2 : 5 with water-cement ratios of 0.50, 0.52, and 0.54 met the expansibility and fluidity requirements for fissure grouting of earthen sites. This combination of a new grouting slurry and optimized grouting technology can solve the problems of detachment due to slurry shrinkage and the need for multiple replenishments.

2. Slurry Preparation and Selection

2.1. Materials and Methods

2.1.1. Material Properties. The main materials used in this research were quicklime, fly ash, crushed earthen site soil, and SH solution. The quicklime was industrial grade lime with a CaO content of 93.6%. The fly ash was grade II, and the main components were SiO₂ (52.2%), Al₂O₃ (31.1%), Fe₂O₃ (3.5%), CaO (2.5%), and MgO (1.7%) with other trace ingredients. The crushed earthen site soil was sampled from the collapsed Great Wall at the experimental site; the soil was silty clay with a water content of 1.53%, natural density of 1.47 g·cm⁻³, compressive strength of 3.50 MPa, tensile strength of 0.61 kPa, cohesion of 32.86 kPa, and internal friction angle of 38.36°. SH is a new type of polymer material (liquid-modified polyvinyl alcohol) developed by Lanzhou University; it has a density of 1.09 g·cm⁻³, and it is highly hydrophilic and soluble in water. Moreover, it is nontoxic

and environmentally friendly, and it has good mechanical properties and a low preparation cost [23, 24].

2.1.2. Experimental Method. In order to determine a suitable grouting slurry with better expansibility and fluidity, nine slurry groups with different ingredient proportions and water-cement ratio were prepared, as given in Table 1. The slurries all used SH solution with a mass concentration of 1.5% as the binder. The proportions of quicklime (CaO), fly ash (F), and site soil (C) followed the mass ratios of CaO : F : C = 1 : 2 : 7, 2 : 2 : 6, and 3 : 2 : 5. The water-cement ratio was determined according to existing results in related research [25, 26] and controlled between 0.48 and 0.54.

Based on JGJ/T70-2009 [27] and BS EN 1015-9:1999 [28], a comparator (standard rod reference length of 176 mm and measurement accuracy of 0.001 mm) and SC-145 pointer mortar consistency meter were used to test the volume expansion ratio and consistency, respectively, of the nine slurry groups.

2.2. Expansibility Tests. The volume expansion ratio of the concretions from the nine slurry groups after 28 d of aging was measured with the comparator. Three parallel samples were used for each group of slurry concretions, and the results were averaged for the final analysis. Table 2 presents the test results. The three water-cement ratios with CaO : F : C = 1 : 2 : 7 and two water-cement ratios of 0.52 and 0.54 with CaO : F : C = 2 : 2 : 6 show negative values for the volume expansion ratios; thus, they did not satisfy the precondition for the slurry to expand.

2.3. Fluidity Tests. After the slurries that did not satisfy the expansion ratio requirement were removed, the remaining four slurry groups were tested for their flow properties. The consistency was measured with a consistency meter, as shown in Figure 1(a), and the test results are shown in Figure 1(b).

- (1) For the ingredient proportion of 2 : 2 : 6 and a water-cement ratio of 0.50, the consistency was 45 mm. Differentiation and segregation occurred after the sample was left standing for 1 h.
- (2) The consistencies of the three water-cement ratios with the ingredient proportion of 3 : 2 : 5 were 59, 67, and 83 mm, respectively. The fluidity of the slurry gradually increased with the water-quicklime ratio. After the samples were left standing for 1 h, no differentiation or segregation occurred.

Therefore, because of the gravimetric and nonpressure grouting methods used for earthen sites and the time factor, the ingredient proportion was set to 2 : 2 : 6. However, the slurry with the water-cement ratio of 0.50 did not meet the fluidity requirement.

2.4. Selection. Based on indoor testing of the nine slurry groups with different ingredient proportions and water-cement ratios, the four groups with the best expansion

TABLE 1: Mixture and water-cement ratios.

No.	Ingredient proportion	Water-cement ratio
1	CaO:F:C = 1:2:7	0.48, 0.50, 0.52
2	CaO:F:C = 2:2:6	0.50, 0.52, 0.54
3	CaO:F:C = 3:2:5	0.50, 0.52, 0.54

TABLE 2: Expansion ratios of different grout concretions over 28 d.

Ingredient proportion	Water-cement ratio	Volume expansion ratio (%)
1:2:7	0.48	-4.11
	0.50	-4.68
	0.52	-8.75
2:2:6	0.50	0.68
	0.52	-2.34
	0.54	-2.52
3:2:5	0.50	6.01
	0.52	5.55
	0.54	4.84

properties were selected for the fluidity test. Based on the required fluidity and reduced shrinkage deformation of the grouting, the final three slurry groups were selected: CaO:F:C = 3:2:5 and water-cement ratios of 0.50, 0.52, and 0.54.

3. Determination of the Curing Age

After the types of grouting slurry were determined, the concretions from the three selected groups were aged for continuous but different periods of time to determine the optimal curing age. Then, they were tested for their compressive, flexural, and tensile strengths.

3.1. Experimental Method. According to GB/T50123-1999 [29], slurries of three water-cement ratios with CaO:F:C = 3:2:5 were used to form 7.07 cm × 7.07 cm × 7.07 cm cubic specimens and 40 mm × 40 mm × 160 mm (width × depth × length) prismatic specimens for curing. According to GB/T17671-1999 [30], the concretion samples cured for 7, 14, 28, 35, 42, 49, 56, 63, and 90 d were then subjected to compressive, tensile, and flexural strength tests [31, 32]. The cubic specimens were subjected to the compressive and tensile strength tests. The compressive strength test was carried out with a CSS-88000 electrohydraulic servo universal testing machine (range: 300 kN) at a loading rate of 1 mm/min. For the tensile strength test, a pair of parallel steel rods was added to the central axis of the upper and lower sides of the cubic specimens and fixed with rubber bands. Then, the CSS-88000 electrohydraulic servo universal testing machine was used to load the specimens at a rate of 3 mm/min until destruction. The prismatic specimens were subjected to the center-point loading flexural test, which was conducted at a fixed rate of 0.1 mm/min with Instron Testing Machine. The prismatic specimens were tested until they were broken into two halves. Then, their flexural strength was computed.

3.2. Test Results. Figure 2 plots the curves of the concretion strength against the curing age.

- (1) The compressive, tensile, and flexural strengths of the concretions gradually increased with the curing time. The growth trends were basically the same for the three water-cement ratios: a fast growth rate early and a relatively slow growth rate later.
- (2) The pressure, tensile, and flexural strength curves all had two inflection points at curing ages of 28 and 63 d. Before 28 d, the intensity curves basically increased linearly, which indicates that the samples quickly grew stronger compared to the initial strength and had good early strength. The intensity growth gradually slowed down and showed an upper-convex curve at curing ages of 28–63 d. After 63 d, the compressive, tensile, and flexural strengths of the concretions were more stable for all specimens and the changes were very slight.
- (3) The sample with the highest strength had the water-cement ratio of 0.50. At 63 d, the compressive, tensile, and flexural strengths were 2.28 MPa, 271 kPa, and 1.75 MPa, respectively, which were 99.1%, 97.5%, and 98.9%, respectively, of the strength at 90 d. This indicates that the slurry had basically completed hardening after 63 d of aging, so a curing age of 63 d was selected.

4. Onsite Fissure Grouting Tests

4.1. Test Site. The onsite fissure grouting experiment was carried out on the rammed earth wall near the Lin-Ze Ming Great Wall in Gansu, as shown in Figure 3. The physical and mechanical properties of the wall soil were generally similar to those of the earthen site, and the rammed wall was complete and stable. Before the experiment, six artificial fissures with a width of 8 cm and depth of 10 cm were cut in the wall. Square holes on both sides of the fissures were scooped for the soundwave test.

4.2. Experimental Materials and Methods

4.2.1. Experimental Materials. The three grouting slurries of SH-(CaO + F + C) with CaO:F:C = 3:2:5 and water-cement ratios of 0.50, 0.52, and 0.54 were used in the field experiment. The lime slurry used for the lime piles was a mixed slurry of 1.5% mass concentration SH solution and quicklime, earthen soil, and polypropylene fiber, where the water-quicklime ratio was 0.75 and the mass ratio of CaO:C was 8:2. The mass ratio of the propylene fiber was 0.5% of the total mass of quicklime and earthen soil.

4.2.2. Experimental Methods. The grouting experimental process was based on WW/T 0038-2012 [33]. Among the six fissures excavated in the experimental wall, the conventional grouting process was adopted for three of them, and no piles were arranged during grouting (Figure 4(a)). The other three fissures were grouted with optimized grouting technology:

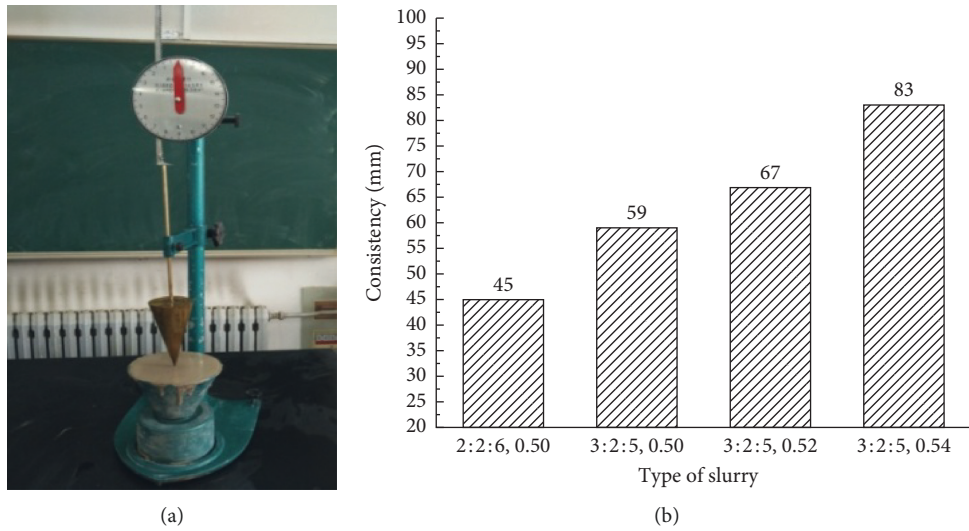


FIGURE 1: Consistency index test: (a) apparatus for the consistency tests and (b) liquidity index for the four slurry groups.

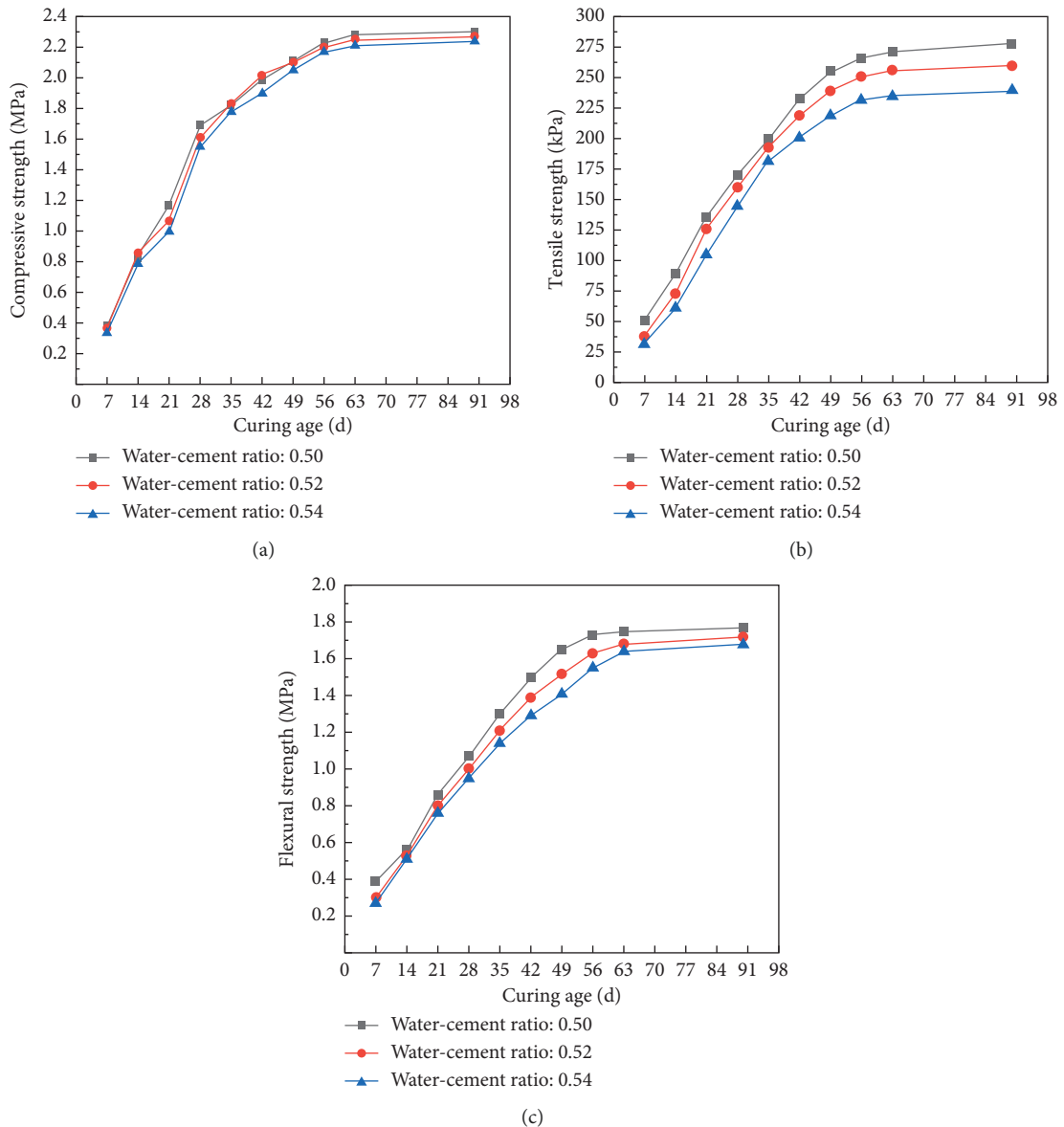


FIGURE 2: Variations in the (a) compressive, (b) tensile, and (c) flexural strengths against the curing age.

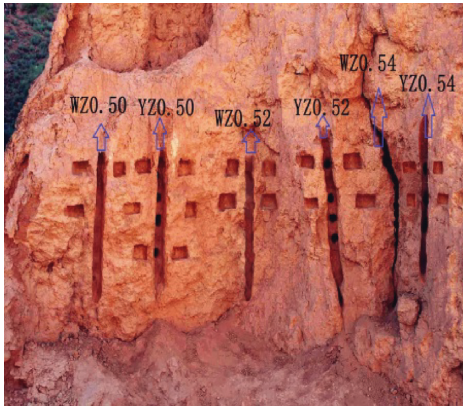


FIGURE 3: Experimental site.

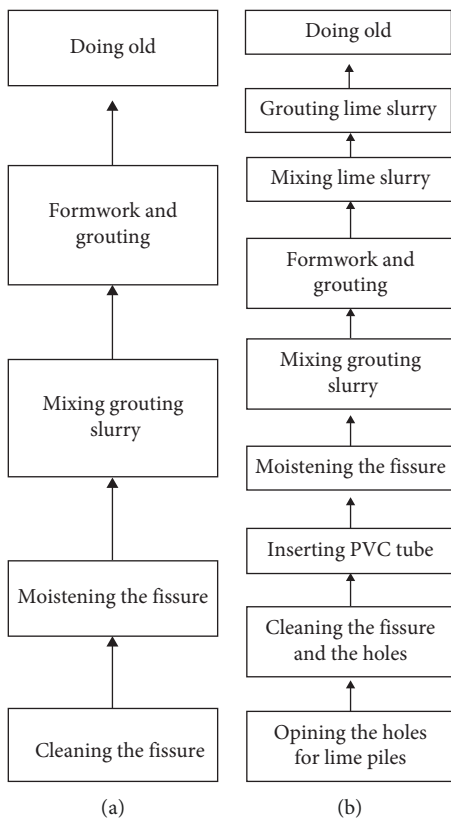


FIGURE 4: Flowcharts of grouting technologies: (a) traditional grouting and (b) optimized grouting with lime piles.

microlime piles were placed in the cracks during grouting (Figure 4(b)).

Depending on whether the grouting process involved lime piles and the water-quicklime ratio of the grouting slurry, the six cracks were labeled as YZ0.50, YZ0.52, YZ0.54, WZ0.50, WZ0.52, and WZ0.54, as listed in Table 3. YZ indicated lime piles, WZ indicated no lime piles, and the number indicated the water-cement ratio of the slurry.

The steps of the traditional grouting process were as follows:

- (1) A small air compressor was used to clean up the floating soil and soil residue in fissures.

- (2) Osmosis reinforcement was sprayed on both sides of the fracture with 1.5% SH slurry.
- (3) The grouting slurry SH-(CaO + F + C) was mixed evenly according to the mixing ratio CaO : F : C = 3 : 2 : 5 and water-cement ratios of 0.50, 0.52, and 0.54.
- (4) Foam board was used as formwork to seal the cracked surface from air.
- (5) Plastic grouting pipes with a diameter of 10 mm were buried at vertical intervals of 300 mm along each crack, which was grouted through the grouting pipe in a bottom-up order. When the grouting pipe overflowed from the adjacent upper grouting pipe, the grouting was stopped and the grouting hole was blocked. Then, grouting was resumed with the above grouting pipe.
- (6) After the slurry had initially set, the mold was removed to allow the concretion to slowly dry.
- (7) The 1.5% SH solution and mud prepared by crushing site soil were used to smooth the surface of the slurry concretion.

The steps of the optimized grouting process were as follows:

- (1) A small drilling machine was used to drill holes in the selected crack of about 20 cm at 10°–15°. The holes were located at the center of the crack. The diameter of a hole was exactly 1.8 times the crack width. The distance between adjacent two holes in a crack was twice the diameter of the hole from the top to bottom.
- (2) A small air compressor was used to clean the floating soil in the holes and crack.
- (3) A PVC pipe with the same diameter as the hole was slowly inserted inside. About 15 cm of the PVC pipe in the wall was exposed.
- (4) 1.5% SH slurry was sprayed on both sides of the fracture as osmosis reinforcement.
- (5) The grouting slurry of SH-(CaO + F + C) was mixed evenly according to the mixing ratio of CaO : F : C = 3 : 2 : 5 and water-cement ratios of 0.50, 0.52, and 0.54.
- (6) Foam board was used as formwork to seal the cracked surface from air and leave only the PVC nozzles exposed.
- (7) Plastic grouting pipes with a diameter of 10 mm were buried at vertical intervals of 300 mm along the crack, and grouting was performed in a bottom-up order. When a grouting pipe overflowed from the adjacent grouting pipe above, the grouting was stopped, and the grouting hole was blocked. Then, the grouting pipe above was used to continue the grouting.
- (8) The 1.5% SH solution was mixed with quicklime, crushed site soil, and polypropylene fiber to form a lime slurry. The water-cement ratio was 0.75, the CaO : C mass ratio was 8 : 2, and the polypropylene

TABLE 3: Fissure grouting field experiment data.

No.	Fissure width (cm)	Grouting slurry	Water-cement ratio	Diameter of the lime piles (cm)	Test method
WZ0.50	8.1	SH-(CaO + F + C)	0.50	No lime piles	Sonic wave monitor
WZ0.52			0.52		
WZ0.54			0.54		
YZ0.50	8.1	SH-(CaO + F + C)	0.50	4.5	Foundation bearing force penetration instrument, infrared thermal imager
YZ0.52			0.52		
YZ0.54			0.54		

fiber mass ratio was 0.5% of the total mass of the quicklime and site soil.

- (9) After the grouting slurry was initially set, the PVC pipe were gently pulled out, and the above lime slurry was injected into the holes under pressure to ensure compactness and fullness.
- (10) After the lime piles and slurry had initially set, the mold was removed so that the slurry concretion and lime pile could slowly dry.
- (11) 1.5% SH solution and mud prepared by crushing site soil were used to smooth the surface of the grout concretion and lime pile.

4.2.3. Test Method. In order to achieve a more reliable quantitative evaluation of the onsite fissure grouting, a sonic wave monitor, infrared thermal imager, and ground bearing force penetration instrument were used to test the wave velocity, penetration resistance, and temperature data of the working area on the rammed wall before and after grouting.

An RSM-SY-type sonic wave monitor was used to test the wave velocity of the rammed wall before grouting, and the mixed wave velocity of the rammed wall and grouting concretion were measured after grouting. From the top to bottom, square holes with a length and width of 10 cm and depth of 7 cm were sequentially excavated on both sides of the fissure. The distance between the square holes and fissure was 5 cm. These holes were convenient for placing the sonic instrument probe. The average values of multiple tests were taken as the final results.

A WG-V-type ground bearing force penetration instrument was used to test the penetration resistance of the same area before and after grouting. The test locations were areas of $0.3\text{ m} \times 0.3\text{ m}$ that were 5 cm away from both sides of the fissure. The measurement points were arranged to follow the piles, which were in the shape of a quincunx. Six points were measured in each area and averaged to obtain the final value.

An R-series research infrared thermal imager was used for the infrared thermal imaging tests of the six experimental fissures. The infrared thermal images were processed and analyzed with Mei-sheng infrared video processing software.

For the analysis, the unit length was selected from the middle axis of the slurry concretion area in the infrared thermal images of each fissure. Second, another unit length parallel to the first one and around 15 cm away was selected from the rammed wall area. Finally, 30 points with a stable temperature were selected from each line, and the average temperature was taken as the final value of the area.

4.3. Grouting Test Results

4.3.1. Macroscopic Morphology of Fissures after Grouting. After curing, the macroscopic morphology of the onsite fissures after grouting was observed. The slurry concretions were dense with both the traditional and optimized technologies and tightly bonded to the soil on both sides of the fissures. No detachment occurred. In addition, the grouting concretion was similar in color to the rammed soils, as shown in Figure 5.

4.3.2. Changes in the Wave Velocity. Figure 6 shows the results of the wave velocity tests.

- (1) With both grouting technologies, the wave velocity clearly improved after grouting. However, the YZ group showed greater amplification at the same water-cement ratio, which indicates that the optimized grouting technology was better at enhancing the strength.
- (2) For the WZ group with the traditional grouting process, the mixed wave velocity of the slurry concretion and rammed wall decreased as the water-cement ratio increased after grouting and curing: 0.952, 0.921, and $0.876\text{ km}\cdot\text{s}^{-1}$. The wave velocity increased to 46.9%, 45.0%, and 32.7%, respectively, compared to that of the rammed wall soil before grouting.
- (3) For the YZ group with the optimized grouting process, the mixed wave velocity after grouting and curing were 0.972, 0.975, and $0.893\text{ km}\cdot\text{s}^{-1}$, which indicate increases of 50.9%, 54.3%, and 36.1%, respectively, compared to that before grouting. The YZ0.52 group had the greatest mixed wave velocity and maximal amplification. This is because the additional lime piles meant that more water was required for strength enhancement during the curing period and the water-cement ratio of 0.52 was most conducive to the strength growth.

4.3.3. Changes in the Penetration Resistance. Figure 7 shows the results of the penetration resistance test.

- (1) For both grouting technologies, the penetration resistance of the rammed soil on both sides of the fissures increased significantly after grouting with different water-cement ratios. This means that the soil was compacted on both sides after grouting, and the strength was improved.



FIGURE 5: Macroscopic shapes of the fissure after grouting: (a) traditional and (b) optimized.

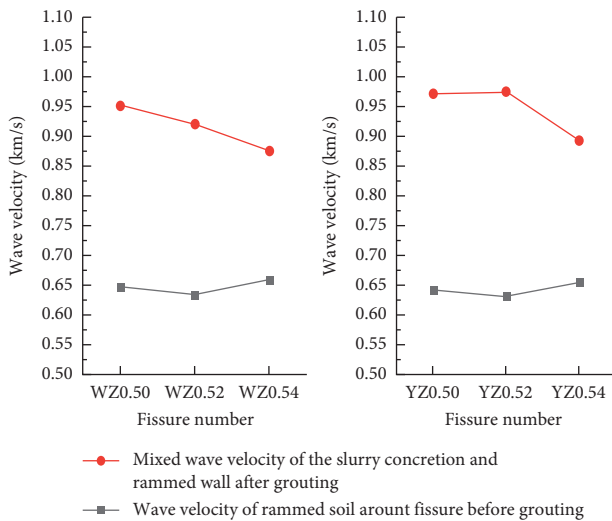


FIGURE 6: Wave velocity test results.

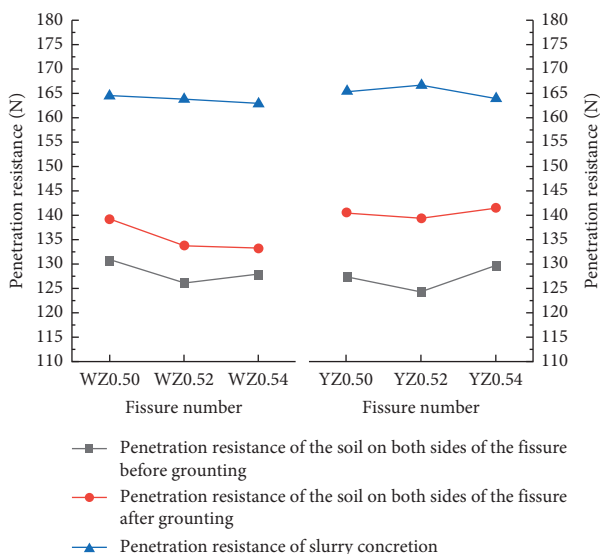


FIGURE 7: Penetration resistance test results.

- (2) For the WZ group with the traditional grouting process, the extent of improvement of the penetration resistance after grouting and curing decreased with an increasing water-cement ratio: 6.4%, 6.0%, and 4.2%. The penetration resistance of the slurry concretions also decreased with an increasing water-cement ratio. This indicates that a lower water-cement ratio allows the soil on both sides of the fissure to be squeezed more easily by the slurry concretion.
- (3) For the YZ group with the optimized grouting process, the penetration resistance increased after grouting by 10.4%, 12.0%, and 9.0% after grouting. The amplification was greatest at a water-cement ratio of 0.52, which corresponds to the trend of the wave velocity.

4.3.4. *Changes in the Temperature.* The infrared thermal imager was used to take photos of the fissures at 13:00–14:00 pm, which are shown in Figure 8. The images show no low-temperature zone between the slurry concretion and rammed soil around the fissures with both grouting technologies, and the transition was relatively gentle. Figure 9 shows the changes in the temperature parameters extracted from the images.

- (1) With both grouting technologies, the average temperature of the concretion in the fissure was lower than the average temperature of the rammed soil around the fissure, but the difference was small. This indicates that the thermal conductivities of these two materials are compatible and will not produce a huge thermodynamic effect at the slurry-soil interface or cause local stress concentrations. That is, the effective bonding at the slurry-soil interface will not be destroyed.
- (2) For the WZ group with the traditional grouting process, the temperature of the slurry concretion decreased as the water-cement ratio increased.
- (3) For the YZ group with the optimized grouting process, the maximal temperature of the concretion

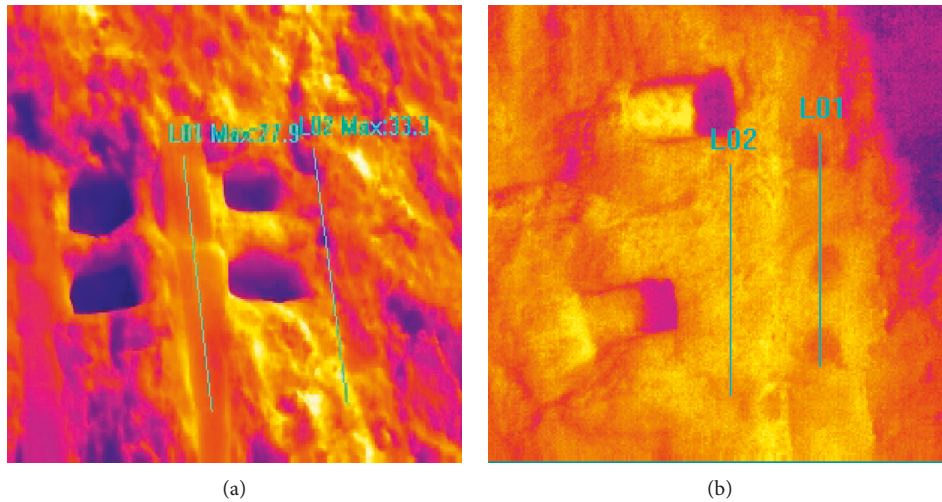


FIGURE 8: Infrared thermograms: (a) traditional grouting and (b) optimized grouting.

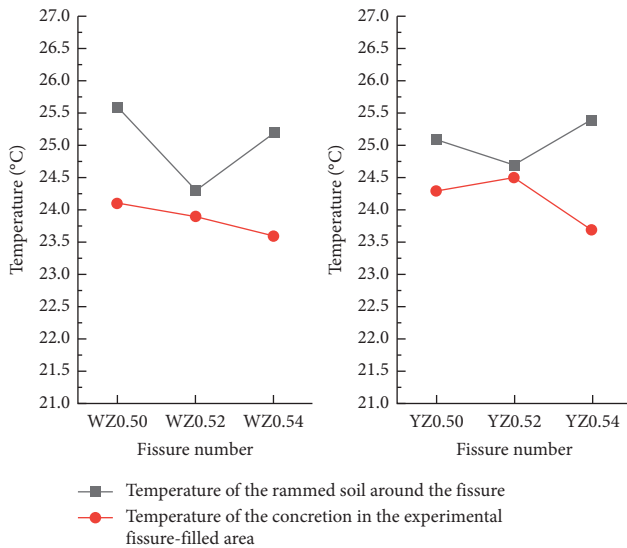


FIGURE 9: Analysis results for the infrared thermograms.

was when the water-cement ratio was 0.52 at 25.4°C. This is because the slurry concretion with a water-cement ratio of 0.52 had the highest dry density. This is consistent with the changes in the wave velocity and penetration resistance, and the thermal conductivity of the concretion body increased with the dry density [34, 35]. Therefore, the YZ group with the water-cement ratio of 0.52 had the highest temperature and was more compatible with the thermal conductivity of the site soil.

5. Analysis and Discussion

The experiments on selecting the slurry and curing age indicated that slurries with an ingredient proportion of $\text{CaO}:\text{F}:\text{C}=3:2:5$ and water-cement ratios of 0.50, 0.52, and 0.54 had typical swelling properties. At 28 d, the concretions experienced no shrinkage but rather volume

expansion ratios of 6.01%, 5.55%, and 4.84%, respectively. This would ensure effective bonding of the slurry-soil interface after grouting and greatly mitigate the problem of large dry shrinkage in the past. The strength-age curves showed that the strengths of the three groups of concretions continued to increase after 28 d and became stable after 63 d. The strengths of the concretions increased rapidly in the first 28 d. During this stage, the hydrolysis and hydration reactions were dominant. The free silica and alumina formed by the hydrolysis and hydration of the fly ash reacted with the calcium hydroxide formed by the hydrolysis of the calcium oxide to produce hydrated calcium silicate and calcium hydrated calcium aluminate under the action of water. Both are hydraulic compounds that can make the slurry quickly turn into cement when the water content is high and produce a certain level of strength. The hydration and dissolution of the lime caused the concretion to swell to satisfy the grouting requirement and enhanced the interfacial bonding ability of the grout. At 28–63 d, the rate of increase of the strength for the slurry concretion slowed down, and the carbonization reaction mainly occurred inside the concretion. The aerobic gelling component, $\text{Ca}(\text{OH})_2$ produced by the hydrolysis of calcium oxide absorbed CO_2 to produce CaCO_3 , which gradually improved the strength of the concretion. After 63 d, the carbonization reaction gradually weakened, and the strength of the slurry concretion no longer improved. The three selected water-cement ratio slurries had small differences in strength at the final curing age (90 d), which indicates that they had good late mechanical strength and stable physical and mechanical properties. These two aspects indicated that the slurries with the three water-cement ratios and $\text{CaO}:\text{F}:\text{C}=3:2:5$ had a typical expansion and hardening mechanism that ensured that the slurry concretion did not shrink after hardening. This solves the problem of shrinkage and detachment. The typical expansion and hardening mechanism was mainly caused by the hydration and carbonization reactions of quicklime and the hydrolysis and hydration reactions of fly ash. This is consistent with the conclusions of Chen et al. [26] and Wang and Xu [36].

The test results for the onsite fissure grouting showed that the slurry concretion could be compacted and then have good contact with soils on both sides of the crack when the optimized technology of arranging microlime piles in the crack was used. This process resulted in good reinforcement. The main functions of the lime pile were as follows:

- (1) Expansion and compaction: in the experiment, the wave velocity in the YZ group with the three water-cement ratios were 4.0%, 9.3%, and 3.4% higher than that of the WZ group, respectively. The penetration resistance in the YZ group was 4.0%, 4.0%, and 4.8% higher than that in the WZ group, respectively. This close agreement showed that the optimized grouting technology is more conducive to grouting reinforcement than the traditional grouting technology. The expansion of the lime piles had an obvious compaction effect on the slurry concretion and the soil on both sides of the fissure. In addition, the width of the experimental fissures was 1.8 times the diameter of the lime piles, so the lime piles had a compacting effect on the slurries within the range of 1.8 times its diameter. This result corresponds to the findings of Mi and Gao [15].
- (2) Heating: when the lime piles were consolidated, along with the reactions of the quicklime, a large amount of heat was released. Then, the free water in the slurry around the lime piles was vaporized to some extent, which promoted the hardening of the slurry concretion.

After the grouting was completed, the slurry concretion and soil on both sides of the crack were effectively bonded without shrinkage and differentiation. In addition to the quicklime, the SH binder also had an effect [37]. When SH is mixed with raw lime, fly ash, and site soil as the binder, this induces adsorption, chemical reactions, and flocculation. SH not only replaces the alkali metal ions but also makes the solid particles of the slurry agglomerate. It can also form hydrogen bonds because of the carboxyl groups on the molecular chain and hydroxyl groups on the surface of the mixture to form a relatively stable structure. The polar hydroxyl group in SH can actively adsorb small particles of the mixture so that the particles are cemented together to form a large polycondensate, which increases the strength of the slurry concretion. After grouting, the SH solution penetrates the soil around the fissure, wraps the soil particles, and forms a mesh-like connection between the particles and pores so that the soil particles form an organic whole. This increases the strength of the soil around the fissure, water stability, and durability. This mesh-like coupling mechanism promotes tight meshing of the slurry particles and soil particles at the slurry-soil interface, which ensures tight bonding without shrinkage or differentiation.

In contrast, the conventional slurry and grouting process caused dry shrinkage to occur after grouting, and secondary cracks formed, as shown in Figure 10. The expansion

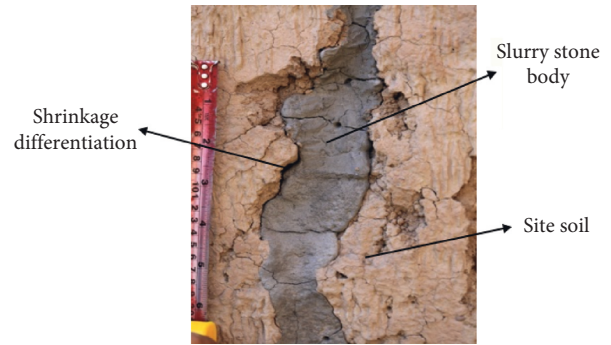


FIGURE 10: Macroscopic morphology of fissures after conventional slurry and grouting processes.

and hardening mechanism of the optimized slurry and the microlime pile compaction and heating effects of the optimized grouting technology can solve the problems of shrinkage and differentiation at the slurry-soil interface, as shown in Figure 5(b).

6. Conclusions

Based on the results, the following conclusions were drawn:

- (1) The SH-(CaO + F + C) slurry with the ingredient proportion $\text{CaO}:\text{F}:\text{C}=3:2:5$ meets the expansibility and fluidity requirements for grouting. The resulting concretion had a typical expansion and hardening mechanism that solves the large shrinkage problem of the traditional slurry.
- (2) The water-cement ratio directly affects the fissure grouting reinforcement. For the WZ group with the traditional grouting technology, the water-cement ratio of 0.50 had the best reinforcement effect. For the YZ group with the optimized grouting technology, the water-cement ratio of 0.52 provided the best results.
- (3) The onsite fissure grouting tests showed that when the fissure width was 1.8 times the diameter of the lime piles, the piles effectively squeezed and compacted the slurry to produce closer contact with the surrounding soil.
- (4) The expansion and hardening mechanism of the slurry and the compaction and heating effects of the microlime piles can solve the shrinkage and separation of the slurry from the surrounding soil after drying to avoid the need for multiple replenishments.

Data Availability

The data used to support the findings of this study are included within the article.

Conflicts of Interest

The authors declare that there are no conflicts of interest regarding the publication of this paper.

Acknowledgments

The research was funded by the National Natural Science Foundation of China (Grant Nos. 41562015 and 51208245). We would also like to express our gratitude for the support provided by the Program for Changjiang Scholars and Innovative Research Team in the University of Ministry of Education of China (2017IRT17-51).

References

- [1] M.-L. Sun, "Research status and development of the conservation of earthen sites," *Sciences of Conservation and Archaeology*, vol. 19, no. 4, pp. 64–70, 2007, in Chinese.
- [2] E. Fodde, "Traditional earthen building techniques in central Asia," *International Journal of Architectural Heritage*, vol. 3, no. 2, pp. 145–168, 2009.
- [3] A. A. Charnov, "100 years of site maintenance and repair: conservation of earthen archaeological sites in the American Southwest," *Journal of Architectural Conservation*, vol. 17, no. 2, pp. 59–75, 2011.
- [4] A. R. Gallardo and J. M. L. Osorio, "Historical rammed earth structures in Eastern Andalusia: (Spain) the restoration philosophy of the architect Prieto-Moreno," in *Proceedings of the 1st International Conference on Rammed Earth Conservation*, pp. 407–412, Valencia, Spain, June 2012, in Spanish.
- [5] P. A. Jaquin, C. E. Augarde, and C. M. Gerrard, "Chronological description of the spatial development of rammed earth techniques," *International Journal of Architectural Heritage*, vol. 2, no. 4, pp. 377–400, 2008.
- [6] Z.-X. Li, L.-Y. Zhao, and M.-L. Sun, "Deterioration of earthen sites and consolidation with PS material along silk road of China," *Chinese Journal of Rock Mechanics and Engineering*, vol. 28, no. 5, pp. 1048–1052, 2009, in Chinese.
- [7] Z.-X. Li, H.-Y. Zhang, and X.-D. Wang, "The reinforcement research of the ancient earth structure sites," *Dunhuang Research*, vol. 3, p. 117, 1995, in Chinese.
- [8] X.-D. Wang, "New progresses on key technologies for the conservation of Chinese earthen sites in arid environment," *Dunhuang Research*, vol. 6, pp. 6–12, 2009, in Chinese.
- [9] F.-G. He, *Study on fissure grouting reinforcement of cliff of jiaohou ancient city*, Ph.D. thesis, Lanzhou University, Lanzhou, China, 2009, in Chinese.
- [10] Gansu Qinghai Academy of Archaeology, Chinese Academy of Social Sciences, and Qinghai Institute of Cultural Relics and Archaeology, "A brief report on the excavation of the Rahab site in Min-he County, Qinghai, in 2000," *Archaeology*, vol. 12, pp. 12–25, 2002, in Chinese.
- [11] L. Li and L.-Y. Zhao, *Research on Lime Materials in Ancient China*, Cultural Relics Press, Beijing, China, 2015, in Chinese.
- [12] A. Brás and F. M. A. Henriques, "Natural hydraulic lime based grouts—the selection of grout injection parameters for masonry consolidation," *Construction and Building Materials*, vol. 26, no. 1, pp. 135–144, 2012.
- [13] A. Bras, F. M. A. Henriques, and M. T. Cidade, "Effect of environmental temperature and fly ash addition in hydraulic lime grout behaviour," *Construction and Building Materials*, vol. 24, no. 8, pp. 1511–1517, 2010.
- [14] J. Grilo, P. Faria, R. Veiga, A. Santos Silva, V. Silva, and A. Velosa, "New natural hydraulic lime mortars—physical and microstructural properties in different curing conditions," *Construction and Building Materials*, vol. 54, no. 11, pp. 378–384, 2014.
- [15] H.-Z. Mi and C. Gao, "Experimental study of expansive behaviors of quick lime," *Chinese Journal of Rock Mechanics and Engineering*, vol. 31, no. 4, pp. 1253–1256, 2010, in Chinese.
- [16] J.-J. Huang, "Researches on selection of anchor slurry and performance mixed quick lime in earthen ruins," Lanzhou University of Technology, Lanzhou, China, Dissertation, 2018.
- [17] J. Liu, "The study on the performance of fissure grouting material and grouting process to the soil ruins in the north-west region," Dissertation, Lanzhou University, Lanzhou, China, 2017, in Chinese.
- [18] L. Li, L.-Y. Zhao, J.-H. Wang et al., "Study on the physical and mechanical properties of two kinds of China ancient buildings," *Chinese Journal of Rock Mechanics and Engineering*, vol. 30, no. 10, pp. 2120–2127, 2011, in Chinese.
- [19] L.-Y. Zhao, L. Li, Z.-X. Li, and J.-H. Wang, "Research on two traditional silicate materials in China's ancient building," *Journal of Inorganic Materials*, vol. 26, no. 12, pp. 1327–1334, 2011.
- [20] A. Kalagri, A. Miltiadou-Fezans, and E. Vintzileou, "Design and evaluation of hydraulic lime grouts for the strengthening of stone masonry historic structures," *Materials and Structures*, vol. 43, no. 8, pp. 1135–1146, 2010.
- [21] L. G. Baltazar, F. M. A. Henriques, and F. Jorne, "Optimisation of flow behaviour and stability of superplasticized fresh hydraulic lime grouts through design of experiments," *Construction and Building Materials*, vol. 35, pp. 838–845, 2012.
- [22] R. A. Silva, O. Domínguez-Martínez, D. V. Oliveira, and E. B. Pereira, "Comparison of the performance of hydraulic lime- and clay-based grouts in the repair of rammed earth," *Construction and Building Materials*, vol. 193, pp. 384–394, 2018.
- [23] F.-G. He, W.-W. Chen, W.-F. Han et al., "Correlation of microstructure indices and performance of sand solidified with polymer material SH," *Rock and Soil Mechanics*, vol. 30, no. 12, pp. 3803–3807, 2009, in Chinese.
- [24] Y.-M. Wang, Z.-C. Yang, W.-W. Chen et al., "Strength characteristics and mechanism of loess solidified with new polymer material SH," *Chinese Journal of Rock Mechanics and Engineering*, vol. 24, no. 14, pp. 2554–2559, 2005, in Chinese.
- [25] W.-W. Chen, J. Liu, K. Cui et al., "The comparative study to performance of the earthen sites fissure grouting material PS-(C + F) and SH-(C + F)," *Sciences of Conservation and Archaeology*, vol. 5, pp. 70–76, 2017, in Chinese.
- [26] W.-W. Chen, J. Liu, S.-Y. Gong et al., "Researches on the durability of the SH-(C + F + CaO) slurry applied to reinforce the cracks in earthen sites," *Chinese Journal of Rock Mechanics and Engineering*, vol. A2, pp. 4310–4317, 2016, in Chinese.
- [27] JGJ/T70-2009, *Standard for Test Method of Basic Properties of Construction Mortar*, Ministry of Housing and Urban-Rural Development, Beijing, China, 2009, in Chinese.
- [28] BS EN 1015-9:1999, *Methods of Test for Mortar for Masonry. Determination of Workable Life and Correction Time of Fresh Mortar*, British Standards Institution, London, UK, 1999.
- [29] GB/T 50123-1999, *Standard for Soil Test Method*, China Planning Press, Beijing, China, 1999, in Chinese.
- [30] GB/T 17671-1999, *Method of Testing Cements—Determination of Strength*, China Planning Press, Beijing, China, 1999, in Chinese.
- [31] X.-R. Ren, J.-K. Zhang, N. Wang et al., "Age performance of grout mixed with calcined gingernuts and earthen fabric in anchoring conservation of earthen sites," *Journal of Materials Science and Engineering*, vol. 35, no. 1, pp. 62–66, 2017, in Chinese.

- [32] J.-K. Zhang, W.-W. Chen, Z.-X. Li et al., "Laboratory tests on property and durability of PS-(C + F) slurry used in anchoring conservation of earthen sites," *Chinese Journal of Geotechnical Engineering*, vol. 37, no. 10, pp. 1802–1809, 2015, in Chinese.
- [33] State Administration of Cultural Heritage, *WW/T 0038-2012: Design Specification for Preservation and Reinforcement Engineering of Arid Earthen Sites*, Cultural Relics Press, Beijing, China, 2012.
- [34] D.-X. Zhang, T.-R. Wang, X.-D. Wang et al., "Experimental study of the heat-conduction properties of earthen ruins soil reinforced by potassium silicate," *Chinese Journal of Rock Mechanics and Engineering*, vol. 30, no. 1, pp. 202–207, 2011, in Chinese.
- [35] D. Zhang, T. Wang, X. Wang, and Q. Guo, "Laboratory experimental study of infrared imaging technology detecting the conservation effect of ancient earthen sites (Jiaohe Ruins) in China," *Engineering Geology*, vol. 125, pp. 66–73, 2012.
- [36] D.-X. Wang and W.-Y. Xu, "Research on strength and durability of sediments solidified with high volume fly ash," *Rock and Soil Mechanics*, vol. 33, no. 12, pp. 3659–3664, 2012, in Chinese.
- [37] S.-X. Chai, P. Wang, W.-F. Han et al., "Research on strength and microstructure feature of solidified saline soil in inshore with polymer," *Rock Mechanics and Engineering*, vol. 06, pp. 1067–1072, 2007, in Chinese.